Chapter 6

TULLY-FISHER RELATIONS

Abstract:

The Tully-Fisher (TF) or the luminosity line-width relations for the Eridanus group of galaxies are constructed using the H I rotation curves, and the optical and the near-infrared luminosities. The slopes of the TF relations (absolute magnitude vs log2× rot-vel.) are -7.1 ± 0.9 in the B-band, -10.0 ± 1.1 in the R-band, -10.1 ± 1.5 in the I-band, -11.8 ± 1.5 in the J-band, -11.3 ± 1.8 in the H-band, and -10.9 ± 1.5 in the K-band for a galaxy sample with flat H I rotation curves. The scatter in the TF relations is observed in between 0.5 mag and 0.8 mag. If the TF relations are estimated using the observed baryonic mass (stellar + H I + Helium mass) instead of the stellar luminosity, nearly identical slopes are obtained in the near-infrared bands. The mean baryonic TF (baryonic mass vs log2× rot-vel.) slope is obtained as 4.2 ± 0.7 using the near-infrared data. The non-baryonic cold dark matter models predict a slope of 3, while the baryonic dark matter models predict a slope of 3.5 for the baryonic TF relation. The present size of the sample (20 galaxies) in this study restricts us to make any firm conclusion.

Keywords: Tully-Fisher relations, galaxy groups, H I rotation curves, baryonic mass, dark matter models.

6.1 Introduction

A correlation ($L \propto V_{rot}^{\alpha}$) between the rotation velocity, V_{rot} (or dynamical mass) of spiral disks inferred from the H I line-width and the intrinsic luminosity, L of galaxies was noticed in late 70's and early 80's by a number of investigators (e.g., Roberts 1969, Rogstad & Shostak 1972, Balkowski et al. 1974, Shostak 1975). Tully & Fisher (1977) gave an application of the luminosity-linewidth relation to measure the distances of spiral galaxies. Subsequently the relation was termed as the Tully-Fisher (TF) relation. They demonstrated that using some nearby spiral galaxies for which the distances are known accurately, the luminosity-linewidth relation can be used to infer the absolute distances to clusters of galaxies as well as a value for the Hubble constant. The index α varies from ~ 3 in the optical to ~ 4 in the near-infrared (e.g., Verheijen 2001). The popular and simplistic way of deriving TF relation using the virial theorem and the Freeman's (1970) law (i.e. constancy of disk central surface brightness) may not be appropriate since it has been shown that the central disk surface brightnesses of galaxies are not constant (see Chap. 4) but both low surface brightness and high surface brightness galaxies follow a similar TF relation. It was realized by Tully & Fisher (1977) that the relation should be fundamental to an understanding of the galactic structure.

The Tully-Fisher relation can be attributed to a correlation between the dark matter halo and the total baryonic mass embedded in it since nearly constant rotation velocities in the outer regions of galaxies are believed to be due to dark matter. Such a correlation between the dark matter halo and the amount of baryonic matter is expected from theories of galaxy formation but the very low scatter observed in the TF relations demands a considerable fine tuning of the theoretical parameters (McGaugh & de Blok 1998). Eisenstein & Loeb (1995) explained that the intrinsic properties of the dark matter halos are not expected to be as tightly correlated as is inferred from the observed TF relations. The cold dark matter models of galaxy formation predict $M_{baryon} \sim V_{rot}^{\alpha}$ between the baryonic mass m, and the rotation velocity V. The index α is predicted to be 3 for non-baryonic dark matter (e.g., van den Bosch 2000, Navarro & Steinmetz 2000) and 3.5 for the collisional baryonic dark matter (Walker 1999). The baryonic mass in the form of stars can be estimated by the stellar luminosity provided the stellar mass to light ratios (M^*/L) are known. Bell & de Jong (2001) showed a strong dependence of M^*/L with colors. They estimated M^*/L as a function of color using the spectro-photometric stellar population synthesis models of galaxy evolution. They also obtained

the baryonic TF relation $m_{baryon} \sim V_{rot}^{3.5\pm0.4}$ for the Ursa-Major galaxies. McGaugh et al. (2000) obtained a higher value for the index, $\alpha = 3.98 \pm 0.12$, which Bell and de Jong argued that it could be due to different M^*/L and distance scales used to construct the two relations. Some of these uncertainties in the properties of dark matter halos derived from theories prompt many to believe in alternate theories. One such theory which has gained a wider acceptance in the past one decade is the Modified Newtonian Dynamics (MOND; Milgrom 1983a) which tries to understand the observed universe in terms of the baryonic matter alone. MOND postulates a breakdown of the classical Newtonian dynamics in the limit of small acceleration (see review by Milgrom 2002). McGaugh et al. (2000) demonstrated that slowly rotating galaxies (mostly dwarfs and some low surface brightness galaxies) in the classical luminosity-linewidth relation are systematically under-luminous, however, if stellar and gas mass together is plotted against the rotation velocity both the slow and the fast rotating galaxies follow an identical the so called baryonic TF relation. Such a baryonic TF relation is a natural consequence of the MOND theory (Milgrom 1983b).

The parameters (index α or the slope if the relation is plotted in log-log scale, and the scatter) of the luminosity linewidth (*classical* TF) relation varies between different studies. The difference seems to arise due to selection effects and biases (Giovanelli et al. 1997), differences in the approach to obtain and to correct the two basic observables, the luminosity and the rotation velocity. Tully & Fouque (1985) have described the procedures to make corrections to the TF observables. There are concerns that observed TF slopes may depend upon the types of galaxies (Rubin et al. 1985). The observed scatter may depend upon the sample size. The inclinations of galaxies should be known accurately to obtain the de-projected rotation velocities. The error in the de-projected rotation velocity will be higher for the low inclination systems. Since scatter in the TF relation is estimated in magnitudes (to give it a meaning for the distance determination), the uncertainty in the projected rotation velocity gets multiplied by the slope. For instance, for a slope of 10 ($\alpha = 4$) in the near-infrared, a marginal error of $5°$ in the inclination introduces a scatter of 0.4 mag and 0.05 mag for inclinations of $45°$ and $80°$ respectively. The luminosity is affected due to internal dust extinction in galaxies. The higher optical wavelengths are less affected by the dust extinction, therefore, accurate estimates of the stellar luminosity can be obtained in the near-infrared. The other advantage in working with the near-infrared luminosities is that the total stellar mass in galaxies is dominated by the old stellar population which emits mostly in the near-infrared. Persic et al. (1996) have shown a strong dependence of the shape of the rotation curves on the I-band luminosities of galaxies. They noticed that the galaxies with $M_I < -22.0$, the rotation curves decline up to $\sim 15\%$ of the maximum rotation velocity in their outer regions. The dependence of TF relation on the shapes of rotation curves has been recently brought into attention by Verheijen (2001). For galaxies in the Ursa-Major group, they reported a scatter as low as 0.21 mag in the K-band TF relation, consistent with the measurement uncertainties leaving no scope for any intrinsic scatter in the TF relation. The slopes they obtained are -7.0 ± 0.4 in the B-band, -8.1 ± 0.4 in the R-band, -8.7 ± 0.5 in the I-band, and -10.1 ± 0.5 in the K-band. They also reported that the scatter in the near-infrared TF relation is reduced by ~ 0.04 mag if the flat rotation velocity is used instead of the maximum rotation velocity. This evidence is rather marginal and is significant in only 3 galaxies in his sample. However, the consequences of such a result are important for theories of galaxy formation as Verheijen (1997) noted that "The TF relations seem to reflect a correlation between the potential of the dark matter halo and the stellar mass embedded in that halo, regardless of its distribution", which of course any theory of galaxy formation should explain.

The I-band TF relation in several clusters and groups have been studied by Giovanelli et al. (1997) using H I line-widths and the optical rotation curves. They noticed that the TF relations in the Eridanus, Fornax, and Centaurus groups/clusters have larger dispersion ($\sigma \sim 0.32 - 0.45$ mag) compared to other clusters where σ is typically less than 0.3. The larger scatter implies that there are significant distance uncertainties for galaxies in these three regions, indicating large physical dispersion of galaxies within them. The I-band TF slope for the Eridanus group was reported as -7.88 ± 0.56, which is slightly steeper than their mean slope (-7.6) for all the clusters. Bamford (2002) reported a K-band TF slope and scatter as -10.8 and 0.58 respectively for the Eridanus group.

In this chapter, TF relations are constructed using the H I rotation curves of galaxies in the Eridanus group using the GMRT observations. The H I observations and the data analyses are described in Chap. 3. The photometric data analysis is given in Chap. 4. The near-infrared photometry in the J, H, and K bands are from the *Two Micron All Sky Survey (2MASS)*. The optical R-band

photometric data are from the observations with the State Observatory, Nainital. The I-band CCD data are from Mathewson & Ford (1996). The B-band data is from the ESO-LV photographic survey of galaxies (Lauberts & Valentijn 1989).

6.2   The sample and the error budget

Bernstein et al. (1994) outlined some criteria for galaxies to be included in obtaining the TF relations. They advocated for non-interacting galaxies of types Sb − Sd with steep H I profiles, smooth outer isophotes and without a prominent bar. Galaxies with inclination < 45° are generally not included in TF studies since the error in the de-projected rotation velocity increases with decreasing inclination. For lower inclination systems, errors in the axial parameters of elliptical isophotes generally increases (see Chap. 4). The cut-off at 45° is just an arbitrary choice where a marginal error of 5° introduces a scatter of 0.4 mag (with a TF slope of -10 in the K-band). One would also like to reduce the scatter due to distance uncertainties therefore a group or a cluster may be the right choice. Using so many selection criteria, it will be difficult to make a reasonable sample size in a group. Since we have not carried out a complete survey of the Eridanus group, several of these selection criteria were relaxed.

No selection is made based on the galaxy type, morphology or inclination except that the interacting galaxies (e.g., NGC 1359) are not included. The sample consists of a total of 20 galaxies for which the H I rotation curves are flat or nearly flat in the outer regions. There are 4 galaxies whose rotation curves are rising till the last measured point in their H I rotation curves. These galaxies are not used for estimating the TF parameters. Unfortunately, the photometric data on all galaxies are not available uniformly in all the bands.

The photometric and kinematical properties of the galaxies are given in Tab. 6.1. The description of the columns are as follows:

Column 1 : Name of the galaxy.

Column 2 : The inclination angle as obtained from the tilted ring model (Sect. 3.5.5) or obtained from the R-band optical images (Sect. 4.4.1) in the cases where tilted ring model did not provide a satisfactory fit.

Column 3 : Log_{10}(W); Width W is $2V_{flat}$, the average velocity at the flat part of the inclination-corrected H I rotation curve (Sect. 3.5.5) or $2V_{lmp}$, the velocity at the last measured point (inclination corrected) in the cases where the rotation curves were not flat.

Columns 4 − 9 : Absolute total magnitude in the B, R, I, J, H, and K bands respectively. These magnitudes includes the extrapolated light from the undetected outer fainter regions of the exponential stellar disk as described in Sect. 4.4.3. The total magnitudes are corrected for the Galactic and internal extinction using the methods described in Sect. 4.4.4. All galaxies are assumed to be at an identical distance of 23 Mpc (distance modulus ∼ −31.808).

The error budget is estimated using uncertainties in different measurements. The instrumental magnitudes for Eridanus galaxies are expected to be accurate to within 0.2 mag for intermediate brightnesses ($m \sim 12$ mag) in the R-band (Chap. 4). The accuracy of the 2MASS photometry is 0.1 mag (Jarrett et al. 2000). The high inclination galaxies for which the kinematical parameters are better determined suffer due to uncertain dust extinction corrections in the optical. This problem should be alleviated in the near-infrared bands. There seems to be not much understanding on how much scatter can be due to uncertainties in the internal dust extinction. Verheijen (2001) noted that the scatter is increased by only a marginal ∼ 0.04 mag from the K band to the R-band for a normal spiral sample. Attributing this scatter to dust corrections, it appears that internal dust corrections are fairly well determined. An extra scatter will be there due to the depth of the group. Assuming that the line of sight depth is similar to the extent in the plane of the sky which is about 4 Mpc for the inner region galaxies studied in this study, the scatter will amount to ∼ 0.35 mag at the distance of the group (23 Mpc). There may be a significant contribution to the total scatter due to errors in the inclination angles of galaxies. For a slope of −10 ($\alpha = 4$) in the near-infrared, a marginal error of 5° in the inclination introduces a scatter of 0.4 mag for 45° , 0.2 mag for 60° , and 0.05 mag for 80° inclinations. We estimate the error budget for an intermediate inclination of 60° . Though all the errors may not be truly random in nature, however, we estimate the rms scatter assuming that the errors add up randomly. This combined error is estimated as ∼ 0.5 mag.

Table 6.1: Properties of galaxies in the TF sample

Name	Incl.	log(W)	$\mathbf{M}_B$	$\mathbf{M}_R$	$\mathbf{M}_I$	$\mathbf{M}_J$	$\mathbf{M}_H$	$\mathbf{M}_K$
galaxies with Flat rotation curve								
ESO 482- G 005	84.6	2.205	-17.48	−	−	-17.31	−	−
ESO 482- G 035	51.8	2.374	-18.39	-18.86	-20.03	-20.62	-21.08	-21.45
ESO 548- G 021	88	2.244	-18.26	−	-19.16	-18.47	-18.19	-18.99
ESO 548- G 072	76.9	1.947	-15.58	−	−	−	−	−
ESO 549- G 035	43.5	2.173	-16.35	−	−	−	−	−
IC 1952	81.4	2.427	-19.22	-19.39	−	-21.55	-22.09	-22.19
IC 1953	50.6	2.476	-19.71	-20.18	-20.91	-22.13	-22.68	-23.04
MCG -03-10-041	62.5	2.342	−	-18.25	−	-19.92	-20.44	-20.54
NGC 1309	13.9	2.517	-19.98	-20.03	−	-21.96	-22.52	-22.77
NGC 1325	74.5	2.500	-20.30	-20.69	-21.73	-22.64	-23.18	-23.33
NGC 1345	16.6	2.367	-18.01	-18.23	−	-20.05	-20.83	-20.84
NGC 1347	14.4	2.287	-18.26	-18.18	−	-20.03	-21.37	-21.05
NGC 1371	48.1	2.716	-20.45	-21.12	−	-23.38	-24.00	-24.21
NGC 1385	51.5	2.442	-20.67	-20.97	-21.85	-22.80	-23.41	-23.55
NGC 1390	60.0	2.374	-17.80	-17.82	−	-19.45	-20.15	-20.40
NGC 1414	79.8	2.193	-18.22	-16.95	-18.90	-19.27	-19.68	-20.10
UGCA 068	37.6	2.244	-18.25	-17.57	−	-18.90	-19.15	-19.65
UGCA 077	64.3	2.193	-17.45	-17.30	-18.23	−	−	−
SGC 0321.2-1929	36.2	2.052	−	-15.04	−	−	−	−
NGC 1415	68.6	2.500	-19.40	-20.76	−	-22.82	-23.36	-23.63
Galaxies with rising rotation curves								
ESO 548- G 065	79.6	2.164	-17.25	-16.96	−	-18.29	−	−
ESO 549- G 002	53.1	2.048	-17.28	-17.46	−	-18.33	−	−
IC 1962	79.8	2.216	-18.07	-17.64	-18.70	-18.24	-18.21	-19.41
NGC 1422	79.6	2.169	-18.65	-17.95	-19.81	-20.38	-20.95	-21.16

6.3 Tully-Fisher relations

6.3.1 *Classical* luminosity-linewidth relation

Figure 6.1 shows TF relations in the B, R, I, J, H, and K bands. The data points marked with filled symbols are for galaxies with flat rotation curves in the outer regions. The galaxies with rising rotation curves till the last measured point are indicated by open circles. A least square fit is carried out to obtain the slope (a) and the intercept (b) for an equation $M = a \, log(2 * V_{rot}) + b$. The fit is carried out using only the galaxies for which the flat rotation velocity is available. All data points are given equal weights. The total observed scatter (rms of residuals) is estimated in magnitudes. The TF parameters obtained from the fits are given in Tab. 6.2.

The slopes of the TF relations obtained in the present analysis are comparable to those obtained in other studies (e.g., Verheijen 2001). The TF slopes from this study are -7.1 ± 0.9 in the B-band, -10.0 ± 1.1 in the R-band, -10.1 ± 1.5 in the I-band, -11.8 ± 1.5 in the J-band, -11.3 ± 1.8 in the H-band, and -10.9 ± 1.5 in the K-band. The slopes reported by Verheijen (2001) for the Ursa-Major galaxies are -6.9 ± 0.5 in the B-band, -8.3 ± 0.6 in the R-band, -9.3 ± 0.6 in the I-band, and -11.2 ± 0.7 in the K-band. Giovanelli et al. (1997) reported the I-band slope for the Eridanus group as -7.88 ± 0.56 with a scatter 0.36 mag using single dish H I data and optical rotation curves. Bamford (2002) carried out a study on Giovanelli et al. (1997) sample using the J, H, and K band magnitudes from 2MASS. He reported a slope of -10.8 in the J-band, -10.9 in the H-band, and -11.1 in the K-band without quoting any fitting error. He reported a total observed scatter of 0.57 mag for the Eridanus.

The large scatter in the TF relation for the Eridanus galaxies in various studies (including the near-infrared studies) indicate that the depth of the group is large by ~ 0.4 mag as compared to other clusters studied in the Giovanelli et al. (1997) sample. It probably indicates that the Eridanus group is physically more dispersed than other groups/clusters. Perhaps, it is tied up with the dynamical stage of the Eridanus group where galaxies or small groups are being accreted from outer regions. Therefore, to study the intrinsic scatter in the TF relation (and hence its tightness), groups like Eridanus may not be suitable.

6.3.2 Baryonic TF relation

In Fig. 6.2, the baryonic (stellar + H I + Helium mass) TF relation is plotted. The molecular gas and ionized gas masses of these galaxies are unknown, therefore, the estimated baryonic masses are only lower limits. The total stellar masses are estimated from the (R–J) colors of galaxies using the galaxy evolution models of Bell & de Jong (2001). These models predict a linear relationship between colors of galaxies and stellar M/L ratio. These models allow one to calculate total stellar mass from the stellar luminosity in any wave-band if colors are known. The Helium mass is taken as 1.32 times of the H I mass. A nearly pass-band independent baryonic TF relation is obtained in the R-band and the near-infrared bands as indicated in Fig. 6.2. The slopes of the baryonic TF relations are 3.42 ± 1.06 from the B-band, 4.25 ± 0.70 from the R-band, 2.44 ± 1.2 from the I-band, 4.24 ± 0.70 from the J-band, 4.09 ± 0.67 from the H-band, and 4.08 ± 0.64 from the K-band luminosities. Except in the B-band and in the I-band, the slopes in all the other bands are more or less similar. This may be an indication that the extinction correction in the B-band are not correct. The number of galaxies in the TF relation in the I-band are very few and therefore the derived parameters are of poor statistical significance. The mean slope of the Baryonic TF relation using the R, J, H, and K band luminosities is 4.2 ± 0.7.

The cold dark matter models predict a slope of 3 for the baryonic TF relation (Navarro & Steinmetz 2000) while a model of collisional baryonic dark matter predicts a slope of 3.5 (Walker 1999). The limited scope of the present analysis due to small sample size prevents us to make any firm conclusion. However, nearly identical slopes obtained in different wave-bands indicate that the stellar synthesis models of Bell & de Jong (2001) are quite accurate in predicting total stellar mass to light ratios from stellar luminosities in different bands. McGaugh (2000) obtained a slope of 3.98 ± 0.12 for a sample of galaxies with rotation velocities over a large range ($30 - 300$ km s^{-1}). Bell & de Jong (2001) in their analysis of Ursa-Major data of Verheijen (2001) obtained a slope of 3.5 ± 0.4. It should be noted that all these analysis (including the present one) do not include molecular and ionized gas masses in calculating the total baryonic mass. Also, the stellar mass to light ratios in the models of Bell & de Jong (2001) were calibrated assuming that the disks are maximally supported by

Table 6.2: TF parameters

Band	#	Slope	intercept	Scatter[1]
Classical TF				
B	12	-7.1 ± 0.9	-2.0 ± 2.1	0.54
R	10	-10.0 ± 1.1	5.0 ± 2.6	0.53
I	6	-10.1 ± 1.5	3.6 ± 3.5	0.49
J	10	-11.8 ± 1.5	7.4 ± 3.6	0.73
H	8	-11.3 ± 1.8	5.7 ± 4.2	0.80
K	8	-10.9 ± 1.5	4.5 ± 3.7	0.71
Baryonic TF				
B	10	3.4 ± 1.1	-2.7 ± 2.6	0.25
R	11	4.3 ± 0.7	0.0 ± 1.7	0.27
I	4	2.4 ± 1.2	4.8 ± 2.9	0.11
J	11	4.2 ± 0.7	0.1 ± 1.7	0.27
H	10	4.1 ± 0.7	0.4 ± 1.6	0.28
K	10	4.1 ± 0.6	0.4 ± 1.5	0.29

1. The scatter is the reduced chi-square value of the fit. The scatters for the classical TF relations are in units of magnitude.

rotation. If this is not the case, the baryonic TF relation will become shallow. In addition, inclusion of molecular gas mass component to the total baryonic mass will systematically make galaxies at the lower velocity end to rise upwards in the TF plots since such galaxies are mostly dwarfs and gas rich HSBs. This effect will further make the slope of their baryonic TF relations shallow. With uncertainties in these analysis and incomplete information about the total baryonic mass in galaxies, currently no dark matter models can be ruled out.

6.4   Conclusions

- The TF slopes in the Eridanus galaxies are in general consistent with those obtained in other studies. The value of the index α ($L \propto V_{rot}^{\alpha}$) is 2.8 ± 0.4 in the B-band, 4.0 ± 0.4 in the R-band, 4.0 ± 0.6 in the I-band, 4.7 ± 0.6 in the J-band, 4.5 ± 0.7 in the H-band, and 4.4 ± 0.6 in the K-band.

- The Eridanus group has a larger scatter ($0.5 - 0.8$ mag) compared to other groups and clusters ($0.2 - 0.4$ mag).

- If the large scatter indicate larger physical dispersion of galaxies in the group, the relative distance differences of galaxies in the Eridanus group will be up to ~ 4 Mpc. This is not very surprising as the Eridanus group is loose and has an irregular appearance.

- The models of Bell & de Jong (2001) predict fairly robust total stellar mass to light ratios in different wave-bands using colors of galaxies.

- The value of the index α ($M_{baryon} \sim V_{rot}^{\alpha}$) of the baryonic TF relation is obtained as 4.2 ± 0.7 from the present analysis.
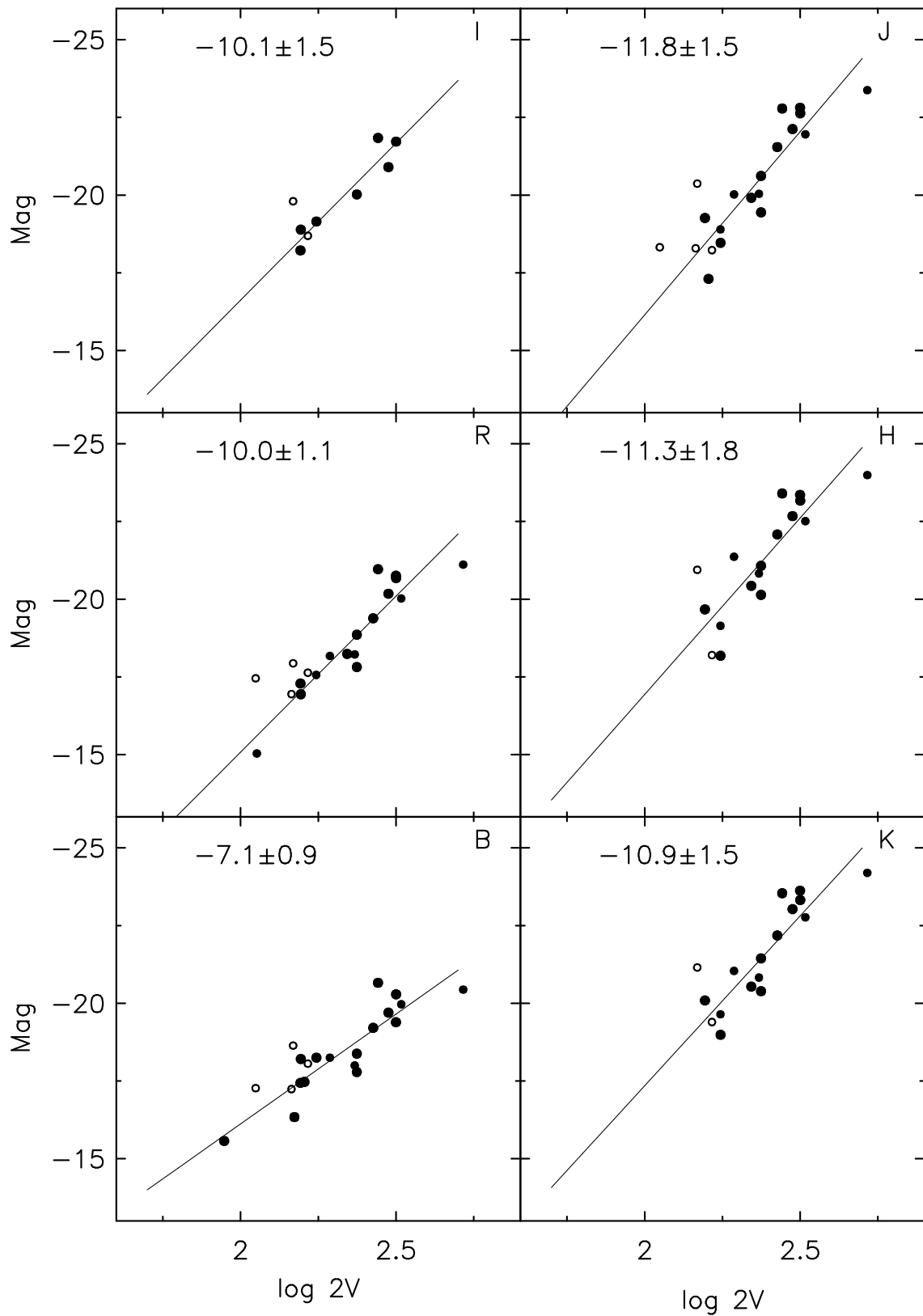
Figure 6.1: The Tully-Fisher relations in different bands. Galaxies marked with filled circles are those with flat rotation curves. Open circles are for galaxies with rising rotation curves till last measured point. The solid line corresponds to the TF relation made using data points marked as filled circles only. The slopes are indicated in each panel.
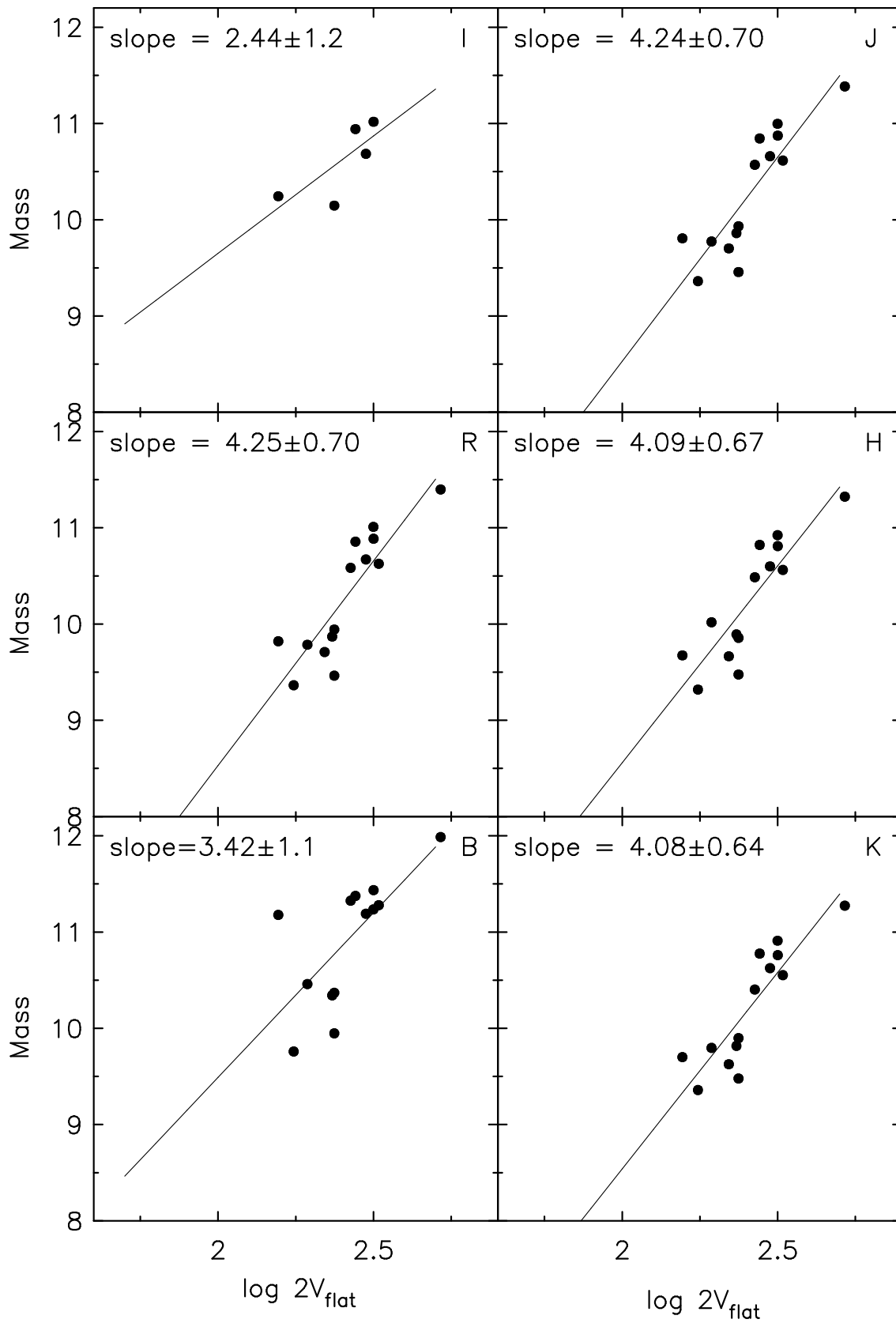
Figure 6.2: The Baryonic (stellar + H I + Helium mass) TF relation. The total stellar mass from each band is estimated using models of Bell & de Jong (2001) and R–J color. A nearly identical TF slope is obtained in the R and the near-infrared bands.

Bibliography

[1] Balkowski, C., Bottinelli, L., Chamaraux, P., Gouguenheim, L., & Heidmann, J. 1974, *A&A*, **34**, 43

[2] Bamford, S.P. 2002, *astro-ph/0210227*

[3] Bell, E.F., & De Jong, R.S. 2001, *ApJ*, **550**, 212

[4] Bernstein, G.M., Guhathakurta, P., & Raychaudhury, S. et al. 1994, *AJ*, **107**, 1962

[5] Freeman, K.C 1970, *ApJ*, **160**, 811

[6] Giovanelli, R., Haynes, M. P., Herter, T., Vogt, N. P., da Costa, L. N., Freudling, W., Salzer, J. J., Wegner, G. 1997, *AJ*, **113**, 53

[7] Jarret, T. H., Chester, T., Cutri, R., Schneider, S., Skrutskie, M., & Huchra, J. P. 2000, *AJ*, **119**, 2498

[8] Lauberts, A. & Valentijn, E.A. 1989, *The Surface Photometry Catalogue of the ESO-Uppsala Galaxies* (Garching:ESO)

[9] Mathewson, D. S., & Ford, V. L. 1996, *ApJ Suppl.*, **107**, 97

[10] McGaugh, S. S., Schombert, J. M., Bothun, G. D., & de Blok, W. J. G.,2000, *ApJL*, **533**, 99

[11] Milgrom, M. 1983a *ApJ*, **270**, 365

[12] Milgrom, M. 1983b, *ApJ*, **270**, 371

[13] Milgrom M. 2002, *New Astron. Review*, **46**, 741

[14] Navarro, J.F., & Steinmetz, M. 2000, *ApJ*, **538**, 477

[15] Persic, M., Salucci, O., & Stel, F. 1996, *MNRAS*, **281**, 27

[16] Roberts, M.S. 1969, *AJ*, **74**, 859

[17] Rogstad, , D.H., & Shostak, G. S. 1972, *ApJ*, **176**, 315

[18] Rubin, V. C., Burstein, D., Ford, W. K., Jr.; Thonnard, N. 1985, *ApJ*, **289**, 81

[19] Shostak, G. S. 1975, *ApJ*, **198**, 527

[20] Tully, R. B., & Fisher, J. R. 1977, *A&A*, **54**, 661

[21] Tully, R.B., & Fouque, P. 1985, *ApJ Suppl.*, **58**, 67

[22] van den Bosch, F.C. 2000, *ApJ*, **530**, 177

[23] Verheijen, M.A.W. 1997, *PhD Thesis, Groningen Univ.*

[24] Verheijen, M.A.W. 2001, *ApJ*, **563**, 694

[25] Walker, M. A. 1999, *MNRAS*, **308**, 551

Chapter 7

RADIO CONTINUUM PROPERTIES

Abstract:

A study of the 1.4 GHz radio continuum emission from galaxies in the Eridanus group is presented. Using the Far-Infrared (FIR) data from the *Infrared Astronomical Satellite* (*IRAS*) and the radio data from the *Northern VLA Sky Survey* (*NVSS*) at 1.4 GHz, the radio-FIR correlation is constructed. Two galaxies, *viz.*, NGC 1407 and NGC 1371 have excess radio emission by more than five times of that expected from the radio-FIR correlation. The radio continuum morphologies obtained from the high resolution GMRT images of these two galaxies show signatures of Active Galactic Nuclei (AGN) related radio emission. Two FIR luminous galaxies, *viz.*, NGC 1377 and IC 1953 are found to be radio-deficient. NGC 1377 ($L_{FIR} \sim 2 \times 10^9$ L$_\odot$) is deficient in the radio continuum emission by more than 40 times of that expected from the radio-FIR correlation. Such galaxies could be having a recent (a few Myr) star-burst. Eridanus lacks in galaxies with 1.4 GHz spectral luminosity exceeding $\sim 10^{22}$ W Hz^{-1}, found mostly in powerful radio galaxies (AGNs) or strong star-bursts. Almost half of the galaxies have star formation rates in the range $0.06 - 0.5$ M$_\odot$/yr. Rest of the galaxies have star formation rates in the range $0.5 - 9$ M$_\odot$/yr. The two most FIR luminous galaxies ($L_{FIR} > 10^{10}$ L$_\odot$) show strong nuclear radio continuum emission typical of that seen in the circum-nuclear star-bursts. The optical morphologies of these two galaxies indicate recent interaction/merger.

Keywords: Radio-FIR correlation, star-burst galaxies, Active Galactic Nuclei (AGN), star-formation rate (SFR), galaxy group, galaxy cluster.

7.1   Introduction

The radio continuum emission from the disks of *normal* galaxies can be due to two physical processes: 1) Synchrotron emission from relativistic electrons in the galactic magnetic field, and 2) Bremsstrahlung (thermal) emission from non-relativistic electrons in the ionized regions. The radio spectral luminosity at 20cm is observed to be tightly correlated with the far-infrared $\lambda \sim 60 - 100\mu$ m luminosity of galaxies (Harwit & Pacini 1975, Condon 1992). This tight correlation (scatter ~ 0.26 dex) is observed in galaxies over a wide range of far-infrared luminosities in the range $10^8 - 10^{12}$ $L_\odot$ (Yun et al. 2001). The origin and the tightness of the radio-FIR correlation is not completely understood.

A possible scenario is an indirect link between the galactic synchrotron and the FIR emission in the disks provided by massive stars. Massive stars (M$> 8M_\odot$) undergo supernova explosions and accelerate electrons to relativistic speeds. Massive stars also heat the dust with their ultraviolet radiation which is re-radiated in the infrared, mostly in the range $\lambda \sim 10 - 300\mu m$. Therefore, a correlation between the radio continuum emission and the far-infrared emission can be expected in this scenario. Most of the scatter in the radio-FIR correlation is believed to be intrinsic in nature. Although strong deviations from the mean radio-FIR correlation are rare, they can be understood as due to either the presence of a black-hole related AGN activities in galaxies (e.g., Roy et al. 1998) in case of a radio-excess, or an early phase of star-bursts (e.g., Roussel et al. 2003) in case of infrared excess in galaxies. The occurrence of either radio excess or infrared excess in galaxies is rather low in a far-infrared selected sample of galaxies. For an example, Yun et al. (2001) found that only 1.3% galaxies have radio excess and only 0.5% galaxies have infrared excess by more than a factor of 5 from the values expected for normal galaxies in a sample of 1809 galaxies with FIR flux greater than 2 Jy. The radio-FIR relation, therefore, can be used to identify AGNs in galaxies or to separate AGNs from star-bursts.

The distribution of radio luminosities of galaxies in a group or a cluster can be interesting for

various reasons. The occurrence of powerful radio source in a cluster can be related to the dynamical state of the cluster (Dwarakanath & Owen 1999). They found in a study of two clusters at similar redshifts that in a loose, dynamically young cluster the galaxy population is dominated by low radio luminosities ($L_{1.4GHz} < 10^{23}$ W Hz^{-1}) which is missing in a virialised cluster. The distribution in 1.4 GHz spectral luminosity is observed to be bi-modal where star-bursts galaxies are separated from the AGN hosting galaxies at a dividing radio luminosity of $\sim 10^{23}$ W Hz^{-1} (e.g., Condon et al. 1989, Yun et al 2001). This criterion can be used to separate AGNs from star-bursts using the radio luminosity. The local environment of galaxies can also affect the radio emission from galaxies. In clusters with high intra-cluster medium density, the magnetic fields in galaxies can be compressed as a result of ram-pressure, thereby increasing the radio emissivity. There are claims that such an effect is observed in some clusters (including Coma, and Virgo) as a radio excess in galaxies which is not due to AGN related activities (e.g., Miller & Owen 2001, Gavazzi & Boselli 1999, Scodeggio & Gavazzi 1993). On the other hand, Menon (1995) reported that spiral galaxies in the high galaxy density regions (e.g., in Hickson groups) have less radio emission as compared to the field spirals. He understood this result as due to depletion of the magnetic field during tidal interactions in high galaxy density groups. The tidal interactions between galaxies can also cause gas from the outer regions of galaxies to flow toward the centre causing circumnuclear star-bursts (Barnes & Hernquist 1992). Most of the strong star-bursts are in fact found to be mergers or strongly interacting.

The Eridanus group seems to be representing an early phase of a cluster formation (Chap. 2, Chap. 5). There is significant sub-clustering in the group where different sub-groups might be merging together to form a cluster (Willmer et al. 1989). The galaxies in the high galaxy density regions are found to be significantly H I deficient (Chap. 5). The deficiency is most likely due to tidal interactions (Chap. 5). The galaxies in the low density regions of the group have normal H I mass expected for field spirals. There is also an increased fraction of S0's in the inner regions. Most of the S0's evolve passively without much star-forming activities as these galaxies have lost most of their gas. The star formation rates (SFR) in galaxies are dependent on the gas surface density in galaxies (Kennicutt 1998). The SFR can be inferred by the FIR emission or by the radio continuum emission. Due to proximity of the Eridanus group, the infrared data from the *Infrared Astronomical Satellite* (*IRAS*; Neugebauer et al. 1984) and the radio continuum data from the *Northern VLA Sky Survey* (*NVSS*; Condon et al. 1998) are sensitive enough to detect most galaxies in the group. Both these data sets can be used to construct the radio-FIR correlation or to obtain the star formation rates in galaxies. The 1.4 GHz GMRT radio continuum data has higher angular resolution ($\sim 4''$) as compared to the NVSS images ($\sim 45''$). The higher angular resolution GMRT images can, therefore, be used to identify any nuclear activity (e.g., AGN, and circum-nuclear star-burst) in galaxies.

In the present study, a radio-FIR correlation for the Eridanus galaxies is constructed using the *IRAS* and the *NVSS* data. Two galaxies (NGC 1407, NGC 1371) are found to be having excess radio emission by more than a factor of five than that expected from the mean radio-FIR correlation. In both the galaxies, linear kpc-scale radio structures typical of those seen in AGNs are found. Some galaxies are found to have significant radio-deficiency (FIR-excess), most notably NGC 1377, an S0 galaxy, has a strong FIR source ($L_{FIR} \sim 2 \times 10^{9}$ L$_\odot$) but no radio continuum emission detected down to $L_{1.4GHz} \sim 6 \times 10^{19}$ W Hz^{-1}, implying a radio-deficiency by more than 40 times of that expected for normal star-burst galaxies. The two (NGC 1482, NGC 1385) most FIR luminous galaxies ($L_{60\mu} > 10^{10}$ L$_\odot$) are identified as due to nuclear star-bursts. The 1.4 GHz spectral luminosity of galaxies is compared with that in other clusters.

7.2 Data analyses

The basic data is obtained from the H I 21cm-line observations of galaxies in the Eridanus group as described in Chap. 3. The channels free of H I line signals were used to obtain the radio continuum images. The details of the observations are described in Chap. 3. The data analyses related to the continuum observations are briefly presented here. The channels free from H I line emission are averaged to make a continuum data set. Images are made using this continuum data, and, *CLEANed*. Self-calibration is carried out to improve the dynamic range. At this stage, no amplitude self calibration is performed. The final self-calibrated and *CLEANed* images are corrected for the primary beam attenuation. All images are regrided to the J2000 epoch. The flux density is scaled using the 3C 48, and 3C 147 flux densities obtained from the VLA calibrator list.

The details of the image properties are given in Tab. 7.1. The total flux densities are estimated

Table 7.1: GMRT image parameters

Galaxy	rms	Resolution	S_{total}	Morph.
	(mJy/bm)	(arcsec)	(mJy)	
NGC 1407	0.50	6×6	99 ± 10	Diffuse
NGC 1371	0.22	15×15	19.7 ± 2	Linear
NGC 1415	0.12	4×4	27 ± 3	Linear
NGC 1482	0.81	8×8	280 ± 30	Diffuse
NGC 1385	0.41	15×15	180 ± 20	Diffuse
NGC 1377	0.20	15×15	$< 1 \, (5\sigma)$	–
IC 1953	0.30	50×45	9 ± 2	Diffuse
NGC 1309	0.35	15×15	68 ± 7	Diffuse
NGC 1345	0.23	32×26	4.5 ± 1	Diffuse
ESO 548-G 036	0.20	16×11	9 ± 1	Diffuse

Notes: Images are natural-weighted. The resolution of each image is such that the diffuse emission is emphasized without losing much of the resolution.

from images at a resolution of $\sim 1'$. The GMRT flux densities are consistent with the NVSS flux densities within 20% for most of the galaxies except for the two weaker ones, viz., IC 1953 and ESO 548- G 036 where the uncertainties are 25% and 30% respectively.

7.3   Results

The 1.4 GHz radio continuum and FIR properties of galaxies are presented in Tab. 7.2. The 1.4 GHz flux densities are from the $NVSS$ and FIR fluxes are from the $IRAS$ faint source catalog. The columns of the table are as follows:

Column 1: Galaxy name.
Column 2&3: The 60μm and 100μm $IRAS$ fluxes.
Column 4: Total FIR luminosity $(8 - 1000\mu$m) estimated using Equ. 7.5.
Column 5: 1.4 GHz flux density from $NVSS$.
Column 6: 1.4 GHz spectral luminosity estimated using Equ. 7.2.
Column 7: Star formation rate estimated using Equ. 7.6.
Column 8: Comments.

7.3.1   Radio-FIR correlation in the Eridanus group of galaxies

A total of 72 Eridanus galaxies are detected in the Far-infrared $(60 - 100\mu$m) using the $IRAS$ faint source catalog. The 60μm and 100μm flux densities are obtained from the $IRAS$ catalog. The IRAS faint source catalog has a limiting sensitivity of ~ 0.3 Jy at 60μm wavelength. The 60μm fluxes are converted to the luminosities using the relation:

$$log L_{60\mu m}(L_\odot) = 6.014 + 2log D + log S_{60\mu \; m} \qquad (7.1)$$

(Yun et al. 2001); where $L_{60\mu m}$ is the 60μm luminosity, D is the distance in Mpc, and $S_{60\mu m}$ is the 60μm $IRAS$ flux density in Jy. At the distance to the group (23 Mpc), the limiting sensitivity of the $IRAS$ observations is $L_{60\mu m} \sim 10^8$ L$_\odot$.

The 1.4 GHz radio flux densities of galaxies are obtained from the $NVSS$ made at a resolution of $45''$ (~ 5 kpc). The $NVSS$ images have an rms of 0.5 mJy/beam. At the distance to the group of 23 Mpc, the 5σ sensitivity limit to the 1.4 GHz radio spectral luminosity is $\sim 2 \times 10^{20}$ W Hz^{-1}. The 1.4 GHz spectral luminosity is estimated using the relation:

$$log L_{1.4GHz}(W Hz^{-1}) = 20.08 + 2log D + log S_{1.4GHz} \qquad (7.2)$$

(Yun et al. 2001); where $L_{1.4GHz}$ is the 1.4 GHz radio spectral luminosity, D is the distance in Mpc, and $S_{1.4GHz}$ is the 1.4 GHz radio flux density in Jy.

Figure 7.1 shows the radio-FIR correlation in the Eridanus group of galaxies constructed using the $IRAS$ and the $NVSS$ flux densities. A total of 72 galaxies are plotted in this figure with their

known FIR fluxes, out of which only 38 galaxies are detected at 1.4 GHz with the $NVSS$. The 5σ limits (log $L_{1.4GHz} < 20.2$) for the radio non-detected galaxies are plotted. In the upper panel of this figure, the straight line corresponds to a unity slope and an intercept of 12.07 W Hz^{-1} as obtained by Yun et al. (2001). The lower panel of this figure shows the q parameter of Condon et al. (1991) to identify the radio-excess or the radio-deficient (FIR-excess) galaxies. This q parameter is estimated using the following relation:

$$q = log\left(\frac{FIR}{3.75 \times 10^{12} Wm^{-2}}\right) - log\left(\frac{S_{1.4GHz}}{1.0 \times 10^{26} Wm^{-2}Hz^{-1}}\right) \qquad (7.3)$$

Condon et al. (1991); where $S_{1.4GHz}$ is the 1.4 GHz radio flux density in Jy, and FIR is estimated from the relation:

$$FIR = 1.26 \times 10^{-14} \left(2.58S_{60\mu m} + S_{100\mu m}\right) Wm^{-2} \qquad (7.4)$$

Helou et al. (1988); where $S_{60\mu m}$, and $S_{100\mu m}$ are $IRAS$ 60μm and 100μm flux densities in Jy.

In the lower panel of Fig. 7.1, the two dotted lines mark three times radio excess (above the mean) or FIR excess (below the mean). The mean value shown by the solid line is at $q = 2.34$ as obtained by Yun et al. (2001). Two galaxies with radio excess (three times below the mean), and 4 galaxies with FIR excess (three times above the mean) are encircled in Fig. 7.1. Rest of the galaxies follow radio-FIR correlation within a maximum scatter of 0.47 dex. A hint of the non-linearity is noticed at FIR luminosity below 10^9 L$_\odot$ as has been previously observed by Yun et al. (2001).

7.3.2   Radio continuum morphologies

A collage of the 1.4 GHz radio continuum images from the GMRT are shown in Figs. 7.2 & 7.3. All the galaxies shown in this collage are in the inner (4 Mpc) regions of the group where the GMRT observations were carried out. It is noticed that several galaxies (NGC 1371, NGC 1407, NGC 1482, NGC 1385, NGC 1415, ESO 548- G 036, IC 1953, and NGC 1345) have nuclear radio continuum emission. The disk radio continuum emission from NGC 1309 and IC 1953 appears to be associated with the spiral arms.

Radio excess galaxies: Evidences for AGN activities

A radio-excess in galaxies can be due to the presence of AGN related activities. In a study of FIR selected radio-excess galaxies, Roy et al. (1999) proposed that most of the radio-excess galaxies should have kpc scale radio structures. Their results were based on high angular resolution (pc-scale) VLBI observations of some radio-excess galaxies. They found that the radio excess galaxies do not follow the radio-FIR correlation even after removing the nuclear component, implying that most of the excess radio emission must be diffuse and on kpc scales which can not be detect in a VLBI observation. In the Eridanus group, two galaxies (NGC 1407, and NGC 1371) have significant radio excess (Fig. 7.1). The 1.4 GHz radio morphologies of these two galaxies from the GMRT are shown in Fig. 7.2. Both the galaxies have kpc-scale radio emission with a bright nuclear continuum source and symmetric diffuse emission around it. Such features are indicating a low luminosity active galactic nuclei in these two galaxies.

NGC 1407 is the most optically luminous (L$_B$ = 4 $\times$ 10^{10} L$_\odot$) galaxy of the group. It is an elliptical (E0) galaxy with X-ray emission (L$_x \sim$ 3 $\times$ 10^{41} erg/s). NGC 1407 is a member of the sub-group which is rich in early type galaxies with 70% population of E+S0 galaxies. A part of the diffuse X-ray emission (see Fig. 2.4, Chap. 2) could be due to the intra-group medium. The 1.4 GHz GMRT flux density is 99 $\pm$ 3 mJy which is in agreement with the $NVSS$ flux density (95 $\pm$ 3 mJy). The 5 GHz radio flux density of NGC 1407 is 44 mJy (Disney & Wall 1977), implying a radio spectral index α ($S \propto \nu^\alpha$) of -0.6. The corresponding 1.4 GHz spectral luminosity is $\sim$ 6 $\times$ 10^{21} W Hz^{-1}. This radio emission is in excess by more than 70 times of that expected from the radio-FIR correlation. At the resolution of 6$''$.0 $\times$ 6$''$.0 ($\sim$ 0.7 kpc), the radio emission is resolved. The GMRT radio continuum morphology consists of a linear structure oriented roughly in the E-W direction (Fig. 7.2). The morphology of this kpc-scale radio emission is similar to found in other low luminosity active galactic nuclei.

NGC 1371 is an early type (Sa) galaxy with a large optical size (D$_{B25} \sim$ 38 kpc). The galaxy is bulge dominated with faint spiral arms in the outer regions. The total blue band luminosity is 2 $\times$ 10^{10} L$_\odot$. It has five times excess radio emission. In the Hα image of NGC 1371 (Hameed & Devereux 1999), four types of emission can be seen 1) HII regions in the spiral arms, 2) weak diffuse
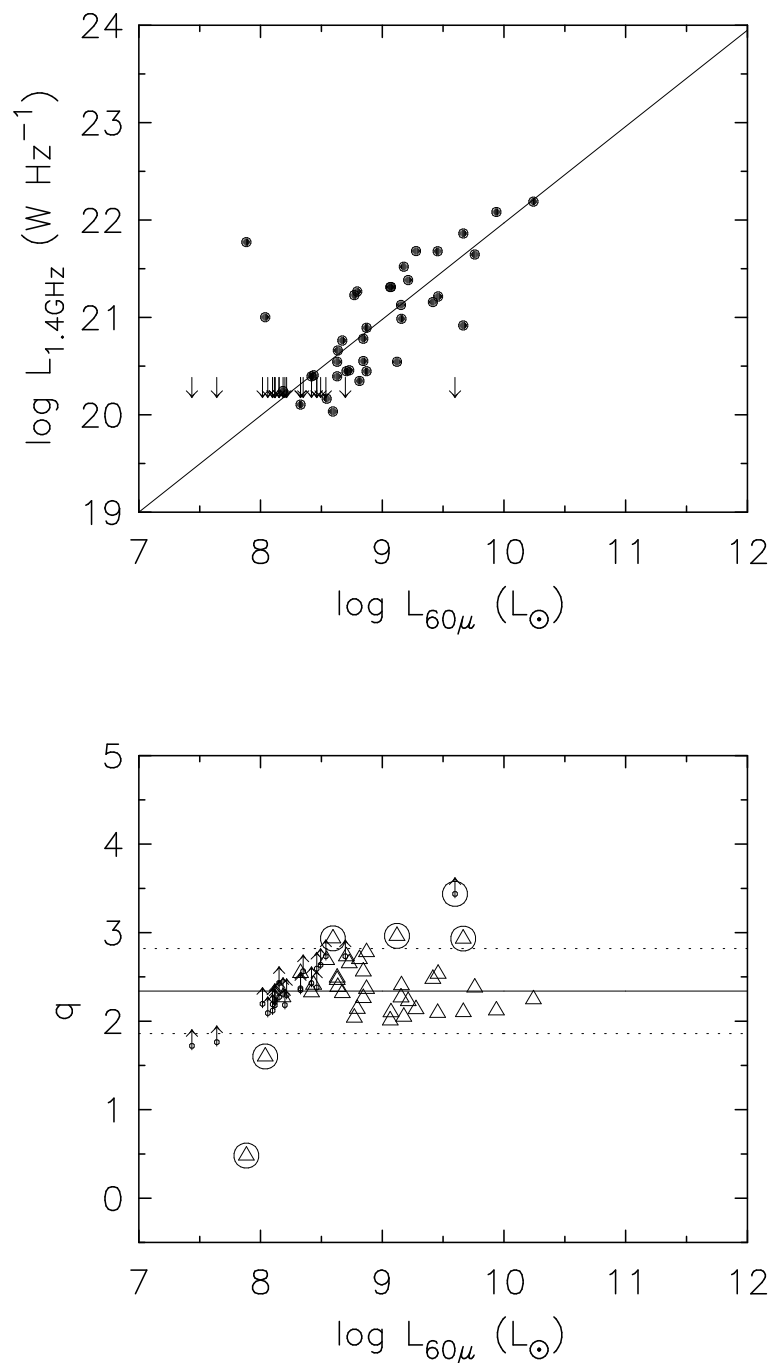
Figure 7.1: (Upper panel) The radio-FIR correlation in the Eridanus group of galaxies constructed using the IRAS 60μm flux and NVSS 1.4 GHz flux densities. The slope, and the intercept of the straight line are 1, and 12.07 W Hz^{-1} respectively as obtained by Yun et al. (2001). (Lower panel) The q parameter (Equ. 7.3) is plotted as a function of the 60μm luminosities of galaxies. The solid line is at $q = 2.34$, the mean value of q obtained by Yun et al. (2001). Two dotted lines indicate three times radio excess (bottom) or three times radio deficit (up) from the mean (centre). The encircled points indicate galaxies having either radio excess or FIR excess by more than 3 times the mean value.
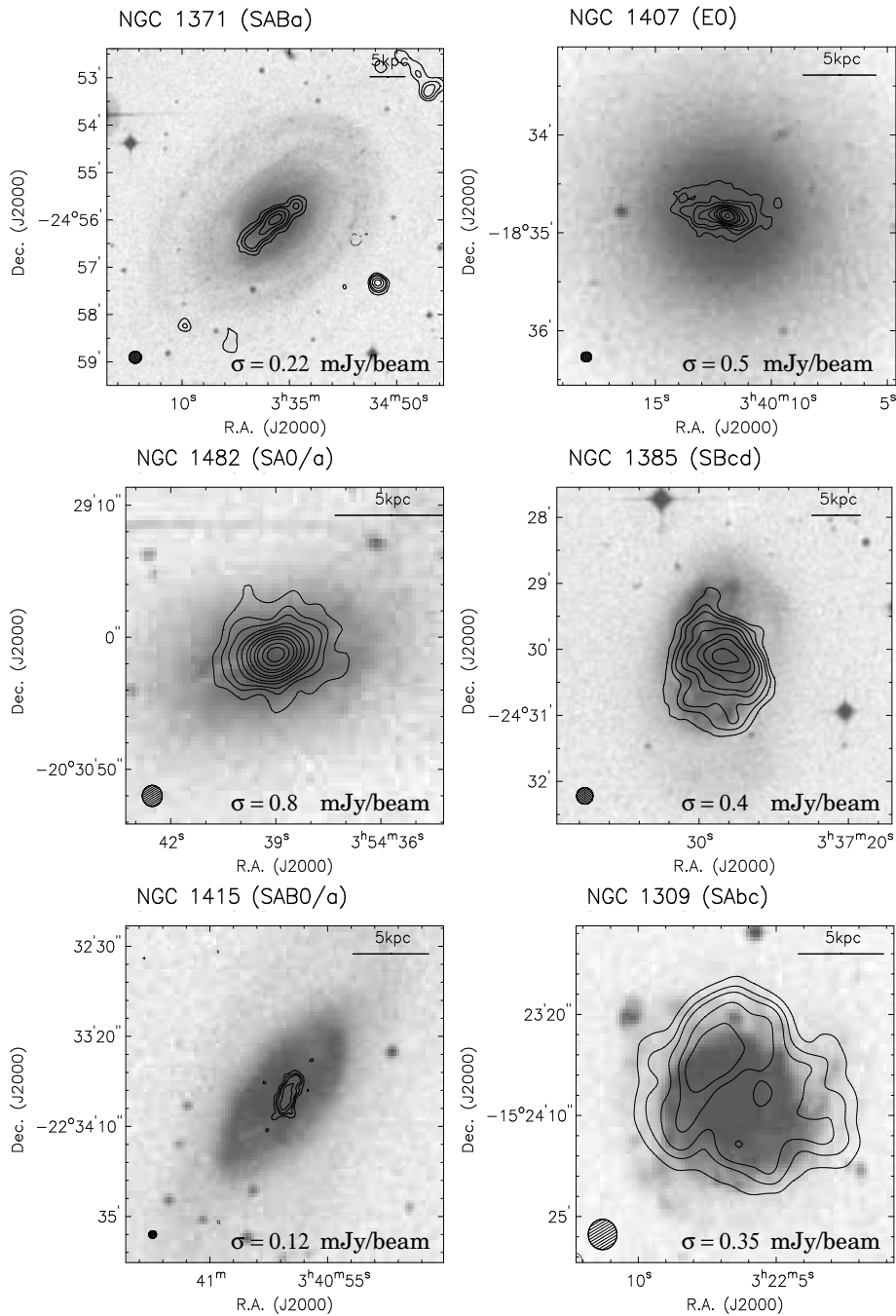
Figure 7.2: A collage of GMRT radio continuum images (in contours) at 1.4 GHz overlaid upon the optical images. The contours start at 3 times the rms value (σ) indicated in the map, and increases in steps of 4.5, 6, 9, 12, 18, 24, 36, 48, 72 $\times \sigma$..
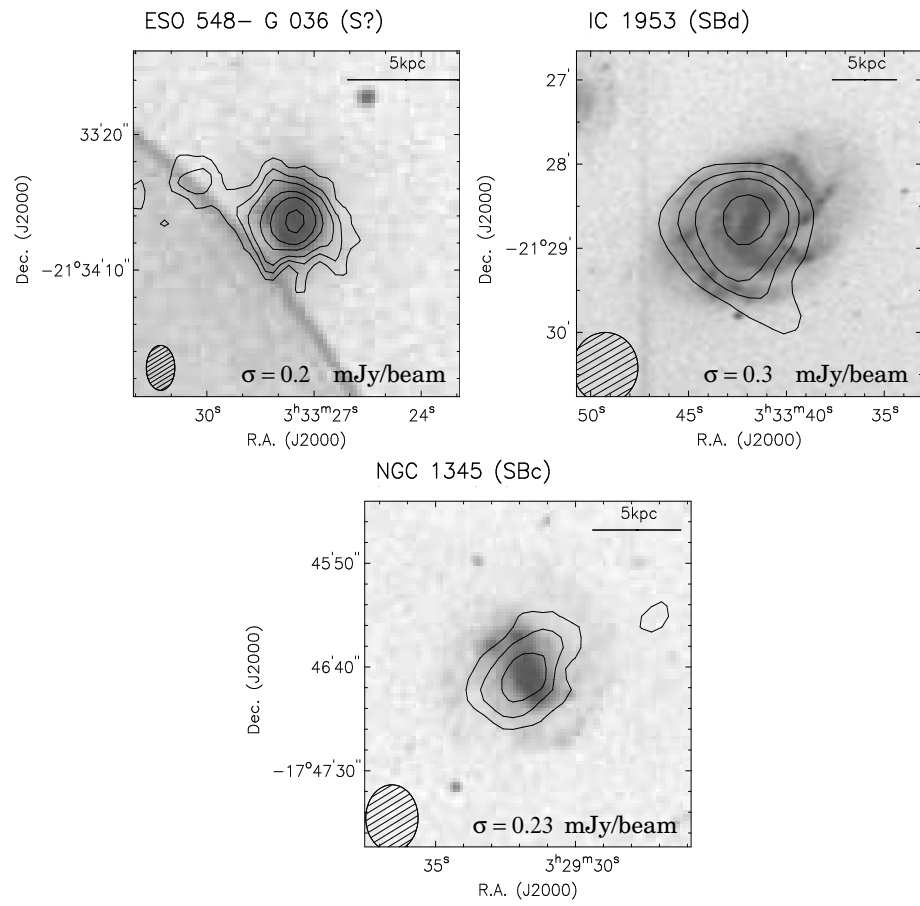
ESO 548– G 036 (S?)

IC 1953 (SBd)

NGC 1345 (SBc)

Figure 7.3: Same as in Fig. 7.2

emission in the bulge, 3) a nuclear point source, and 4) a nuclear ring. The total Hα luminosity of NGC 1371 is 4.9×10^{40} erg/s which is at the faint end of the Hα luminosities of early type galaxies in their sample. The radio morphology of NGC 1371 (Fig. 7.2) shows a linear radio structure which could be due to a jet from the centre. The bright radio point source in the centre is coincident with the bright Hα nuclear point source. No Hα feature similar to the radio morphology is seen, indicating the radio emission could be due to an AGN. The apparent alignment of the jet with the major axis of NGC 1371 we believe is a projection effect although in reality the jet is at a large angle from the plane of the galaxy.

FIR luminous galaxies

The Eridanus group has two galaxies (NGC 1482, NGC 1385) with $60\mu m$ luminosity greater than 10^{10} $L_\odot$, typical of star-burst galaxies. Both galaxies are in the outer regions (> 4 Mpc) of the group. NGC 1482 is an early type disk (S0/a) galaxy, and NGC 1385 is an Scd galaxy. The FIR luminosity can be used to infer a star formation rate ($SFR = 1.7 \times 10^{-10} L_{8-1000\mu m}$, Kennicutt 1998) with an uncertainty of 30%, in the star-bursts galaxies. The $L_{8-1000\mu m}$ can be obtained from the relation:

$$L_{8-1000\mu} = f. (1 + 0.387 S_{100\mu m}/S_{60\mu m}) L_{60\mu m} \qquad (7.5)$$

(Helou et al. 1988); The factor f is found to be in between 1.2 and 2.0 for star-burst galaxies (Sanders 1991). Adopting a value of 1.6 for f, total FIR ($L_{8-1000\mu}$) luminosity of NGC 1482 and NGC 1385 are 4.0×10^{10}, and 2.6×10^{10} $L_\odot$ respectively. The corresponding star formation rates are ~ 7, and ~ 4 $M_\odot$/yr for NGC 1482 and NGC 1385 respectively. The star formation rates can also be estimated using the relation which is derived from the radio-FIR correlation:

$$SFR \sim 6 \times 10^{-22} L_{1.4GHz} WHz^{-1} \qquad (7.6)$$

(Yun et al. 2001); where $L_{1.4GHz}$ is 1.4 GHz spectral luminosity. The SFR estimated from this relation are ~ 9, and ~ 7 $M_\odot$/yr for NGC 1482 and NGC 1385 respectively. The difference between the SFRs estimated from the FIR and the radio flux density is most likely due to uncertainty in the spectral energy distribution in the infrared and the intrinsic scatter in the radio-FIR correlation.

Fig. 7.2 shows the GMRT 1.4 GHz images of NGC 1482 and NGC 1385 overlaid upon the optical images. The 1.4 GHz GMRT flux density is 216 ± 12 mJy consistent with the NVSS flux density (243 ± 15 mJy) within an uncertainty of $\sim 10\%$. NGC 1482 has a dust lane which can be partially seen in Fig. 7.2. The main body of the galaxy is similar to an S0 galaxy. The radio continuum emission from NGC 1482 is oriented roughly along this dust lane. Strong stellar winds from the nucleus has been detected in the Hα (Hameed & Devereux 1999, Veilleux & Rupke 2002). Interestingly, there are ridges in the GMRT radio continuum image at positions corresponding to the outflow seen in the Hα image (cf. Veilleux & Rupke 2002).

The extensions to the radio continuum emission can be seen in the directions perpendicular to the disk. Interestingly, the Hα image of Veilleux & Rupke (2002) shows similar extensions which they attributed to strong stellar winds from the nuclear star-burst. Sanders et al. (1991) have detected $\sim 1 \times 10^9$ $M_\odot$ of molecular Hydrogen toward the centre (~ 100 pc) using the 12m NRAO telescope. Such large amounts of molecular gas in a compact region implies gas density could be of the order of 10^4 $M_\odot$ pc^{-2}. Such high gas densities can result into intense burst of star formation consistent with the high rate of SFR seen in NGC 1482.

NGC 1385 appears to be a disturbed galaxy in the optical images. There is a low surface brightness stellar stream south of the galaxy (Fig. 7.2). The optical morphology near the centre consists of a bar and irregular spiral arms. The overall optical morphology indicates a recent tidal interaction or a merger. The radio continuum morphology (Fig. 7.2) shows diffuse extended emission with extensions roughly along the disturbed spiral arms. The GMRT 1.4 GHz flux density is 140 ± 5 mJy which is somewhat lower than that from the $NVSS$ (190 ± 6 mJy). It could be due to significant (20%) calibration offsets either in the $NVSS$ or in the GMRT data. Elfhag et al. (1996) detected $\sim 8 \times 10^8$ $M_\odot$ of molecular Hydrogen from the nucleus (within 100pc), which could be responsible for the star-burst.

Radio deficient galaxies

Radio deficient, a term which is more appropriate for otherwise known as FIR excess for galaxies having higher values of q compared to galaxies following the radio-FIR correlation. Nine such galaxies were noticed by Yun et al. (2001) for which the FIR/radio ratio (q) exceeds 3. The nature of such galaxies remains elusive until recently when Roussel et al. (2003) showed that such galaxies are
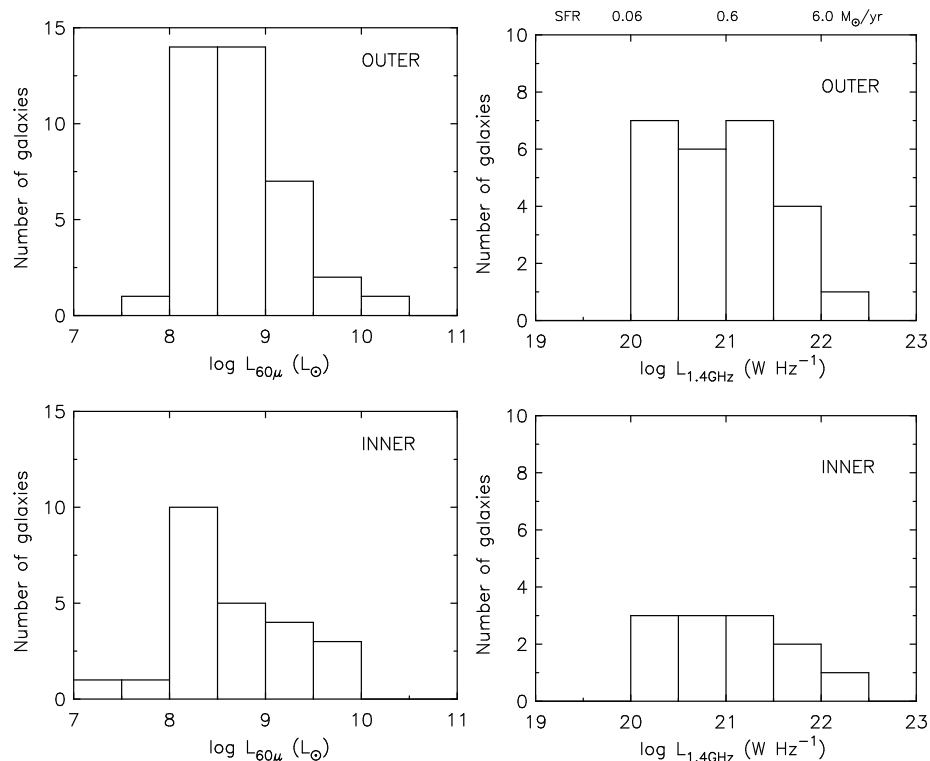
Figure 7.4: Histograms of the FIR luminosity and the 1.4 GHz radio spectral luminosity in the Eridanus group.

undergoing a very recent (< 1 Myr) phase of star-burst. In this scenario, the star-burst is so young that massive stars are heating the surrounding dust, but, have not undergone supernovae explosions. At a level of three times radio deficiency from the mean radio-FIR correlation, four galaxies are noticed in the Eridanus group. Two (NGC 1377, IC 1953) of them were studied by Roussel et al. (2003) for their high FIR/radio ratio. The values of q are ~ 3.4 and ~ 2.9 for NGC 1377 and IC 1953 respectively in Fig. 7.1. The other two galaxies NGC 1353 and NGC 1400, although have FIR/radio ratio comparable to IC 1953, but are of 60μm luminosity lower than 10^9 $L_{\odot}$. Galaxies with lower 60μm luminosities do not follow the radio-FIR correlation, and have excess FIR emission which is believed due to additional heating of dust from the UV flux from the older population of stars (Condon 1992). At higher 60μm luminosities, this UV flux is insignificant as compared to that provided by massive young stars. Therefore, NGC 1353 and NGC 1400 have excess FIR emission which is not related to the young stellar populations.

NGC 1377 is an S0 galaxy with strong FIR emission ($L_{FIR} = 8 \times 10^9$ $L_{\odot}$). It is also a warm IRAS galaxy (60μm peaker) with $S_{60\mu}/S_{100\mu} \sim 1.3$. The warm IRAS galaxies are believed to be due to nuclear star-burst probably triggered by recent interaction or merger (e.g., Heisler & Vader 1995). No radio continuum emission is detected from NGC 1377 either in the NVSS or in the GMRT images. The non-detection in the radio emission down to a 5σ sensitivity of 1 mJy in the GMRT images implies that NGC 1377 is radio deficient by more than 40 times from that expected for normal star-burst galaxies. IC 1953 is an Scd galaxy with grand spiral arms and a prominent bar. The radio continuum morphology consists of a nuclear point source and diffuse emission in the disk. The disk radio continuum emission shows enhancement in the spiral arms. Using high resolution (kpc-scale) mid-infrared images of IC 1953, Roussel et al. (2003) suggested that while the disk radio continuum emission is consistent with the disk infrared emission from the dust, the nucleus lacks in the radio emission for its infrared emission. It is suggestive of a recent nuclear star-burst similar to NGC 1377.

7.3.3 Star formation in the Eridanus group

Histograms of 1.4 GHz radio spectral luminosity and 60μm luminosity of galaxies in the Eridanus group are plotted in Fig. 7.4. The shapes of histograms in the outer and the inner regions of the

Eridanus group are almost identical. However, number of galaxies detected in FIR in the inner region are 26 while that in the outer regions are 39. This difference is mainly due to increased fraction of S0's in the inner regions. The fractions of spiral galaxies detected in FIR in the outer and the inner region are similar, being ~ 0.7 and ~ 0.6 respectively. The star formation rate indicated on the top axis of the upper panel of Fig. 7.4 is estimated using the 1.4 GHz spectral luminosity (Equ. refequ;SFR). It can be noticed that the Eridanus group lacks in galaxies with high radio luminosities ($L_{1.4GHz} > 10^{22}$ W Hz^{-1}). Galaxies higher than this luminosity are generally identified as due to powerful AGN activities (Condon 1989, Yun et al. 2001). There is also a lack of strong star-burst galaxies ($L_{60\mu} > 10^{10}$ L$_\odot$) in the group. Majority (50%) of galaxies have star formation rates in the range $0.06 - 0.5$ M$_\odot$/yr. Rest of the galaxies have star formation rates in the range $0.5 - 9$ M$_\odot$/yr.

7.4 Summary and Conclusions

The main results from the radio continuum study of galaxies in the Eridanus group are:

1) The Eridanus galaxies follow the well-known radio-FIR correlation.

2). The two star-burst galaxies (NGC 1482, NGC 1385) with $L_{60\mu} > 10^{10}$ L$_\odot$ show evidences of nuclear star-burst which could be due to a merger or strong tidal interaction in the past.

3). The two galaxies (NGC 1407, NGC 1371) with significant radio excess are identified as radio AGNs.

4). Two FIR luminous galaxies (IC 1953, NGC 1377) are found in the group which have significant radio deficiency. These galaxies are most likely in a very recent phase of star-burst.

5). About half of the galaxies in the group have star formation rate in the range $0.06 - 0.5$ M$_\odot$/yr.

6). The group lacks in strong AGNs as found in some clusters of galaxies.

Table 7.2: FIR and radio properties of galaxies

Name	$S_{60\mu}$ (Jy)	$S_{100\mu}$ (Jy)	$\log L_{FIR}$ ($L_\odot$)	$S_{1.4}$ (mJy)	$\log L_{1.4}$ (W Hz^{-1})	SFR ($M_\odot$/yr)	Comment
NGC 1300	2.75	10.3	9.77	52.1	21.52	1.96	
UGCA 068	0.21	0.56	8.57	–	< 20.2	< 0.06	
NGC 1325	0.63	3.21	9.21	–	< 20.2	< 0.06	
NGC 1325A	0.24	0.85	8.70	–	< 20.2	< 0.06	
NGC 1332	0.50	1.78	9.02	4.0	20.40	0.15	
NGC 1345	0.78	1.59	9.06	3.9	20.40	0.15	
NGC 1347	0.30	0.99	8.78	–	< 20.2	< 0.06	
ESO 548- G 028	0.29	0.61	8.66	–	< 20.2	< 0.06	
ESO 548- G 029	0.24	0.73	8.66	–	< 20.2	< 0.06	
NGC 1353	2.42	8.79	9.70	5.5	20.54	0.21	FIR-excess
IC 1952	0.79	3.19	9.25	7.2	20.66	0.27	
IC 1953	8.47	11.28	10.05	13.0	20.92	0.49	FIR-excess
NGC 1359	2.13	4.28	9.52	32.2	21.31	1.21	
ESO 548- G 047	0.39	1.00	8.83	–	< 20.2	< 0.06	
NGC 1370	1.19	2.17	9.25	3.5	20.35	0.13	
NGC 1377	7.25	5.74	9.92	–	< 20.2	< 0.06	FIR-excess
NGC 1385	15.87	33.78	10.40	190	22.08	7.13	star-burst
NGC 1395	0.05	0.34	8.20	–	< 20.2	< 0.06	
NGC 1400	0.72	2.50	9.17	1.7	20.03	0.06	FIR-excess
NGC 1407	0.14	0.48	8.45	93.3	21.77	3.50	radio-excess, AGN
NGC 1415	5.27	12.73	9.95	25.8	21.22	0.97	AGN
ESO 482- G 035	0.26	1.00	8.75	–	< 20.2	< 0.06	
NGC 1422	0.39	1.09	8.85	–	< 20.2	< 0.06	
NGC 1439	–	0.34	–	–	–	< 20.2	
NGC 1440	–	1.29	–	–	–	< 20.2	
NGC 1438	0.23	0.79	8.67	–	< 20.2	< 0.06	
NGC 1481	0.36	–	8.50	3.7	20.37	0.14	
ESO 548- G 036	1.94	–	9.23	7.4	20.67	0.28	Polar-ring
ESO 548- G 043	0.35	–	8.49	–	< 20.2	< 0.06	
UGCA 073	0.3	–	8.42	–	< 20.2	< 0.06	
NGC 1145	0.98	3.50	9.31	4.5	20.46	0.17	
NGC 1163	0.64	1.71	9.06	2.3	20.17	0.09	
MCG -03-08-057	0.57	2.39	9.12	–	< 20.2	< 0.06	
NGC 1187	10.54	22.41	10.22	69.6	21.65	2.61	
NGC 1179	0.41	2.21	9.04	–	< 20.2	< 0.06	
NGC 1231	0.23	0.58	8.60	–	< 20.2	< 0.06	
MRK 1069	1.28	1.86	9.24	9.5	20.78	0.36	
NGC 1232	3.47	21.7	10.02	75.5	21.68	2.83	
IC 1898	0.78	2.77	9.21	5.5	20.54	0.21	
NGC 1255	2.99	11.36	9.81	38.0	21.38	1.43	
NGC 1258	0.28	1.09	8.79	–	< 20.2	< 0.06	
NGC 1292	1.36	4.38	9.43	4.4	20.45	0.17	
UGCA 064	0.19	0.91	8.68	–	< 20.2	< 0.06	
NGC 1302	0.26	1.74	8.91	–	< 20.2	< 0.06	
NGC 1306	2.63	4.73	9.59	15.2	20.99	0.57	

Name	$S_{60\mu}$ (Jy)	$S_{100\mu}$ (Jy)	$\log L_{FIR}$ ($L_\odot$)	$S_{1.4}$ (mJy)	$\log L_{1.4}$ (W Hz^{-1})	SFR ($M_\odot$/yr)	Comment
IRAS 03191-2456	0.53	0.78	8.86	–	< 20.2	< 0.06	
NGC 1309	5.22	14.26	9.97	75.2	21.68	2.82	
UGCA 071	0.28	0.81	8.71	2.76	20.24	0.10	
NGC 1338	1.36	4.95	9.46	12.3	20.89	0.46	
ESO 481- G 029	0.48	1.16	8.91	–	< 20.2	< 0.06	
ESO 418- G 008	0.48	1.22	8.92	3.9	20.40	0.15	
NGC 1357	0.93	4.67	9.38	4.4	20.45	0.17	
NGC 1371	0.20	1.36	8.80	15.8	21.00	0.59	radio-excess, AGN
NGC 1398	1.14	8.96	9.60	29.0	21.27	1.09	
NGC 1425	1.08	5.89	9.47	26.6	21.23	1,00	
NGC 1421	8.48	21.32	10.16	114.5	21.86	4.30	
MCG -02-10-009	0.53	2.13	9.07	–	< 20.2	< 0.06	
MCG -03-10-042	0.86	3.40	9.28	9.1	20.76	0.34	
034559-1231	0.63	1.68	9.05		< 20.2	< 0.06	
MCG -03-10-045	4.77	7.88	9.83	22.6	21.16	0.85	
NGC 1461	0.08	0.31	8.24	–	< 20.2	< 0.06	
UGCA 085	0.24	0.93	8.72	–	< 20.2	< 0.06	
NGC 1464	2.61	4.89	9.59	21.1	21.13	0.79	
NGC 1482	31.95	45.32	10.63	243	22.19	9.12	star-burst
IC 2007	1.28	2.77	9.31	5.6	20.55	0.21	
NGC 1518	2.16	6.55	9.61	32.3	21.31	1.21	
NGC 1519	0.91	2.48	9.21	–	< 20.2	< 0.06	
ESO 483- G 013	0.39	1.08	8.85	2.0	20.11	0.08	
J041343-1729	0.98	1.77	9.16		< 20.2	< 0.06	
ESO 550- G 008	0.17	–	8.17	–	< 20.2	< 0.06	
UGCA 061	0.19	–	8.22	–	< 20.2	< 0.06	
IRAS 03007-1531	0.36	–	8.50	–	< 20.2	< 0.06	

Bibliography

[1] Barnes, J.E., & Hernquist L. 1992, *ARA&A*, **30**, 705

[2] Condon, J.J. 1989, *ApJ*, **338**, 13

[3] Condon, J.J., Anderson, M.L., & Helou, G. 1991, *ApJ*, **376**, 95

[4] Condon, J. J. 1992, *ARA&A*, **30**, 575

[5] Condon, J. J., Cotton, W. D., Greisen, E. W. et al. 1998, *AJ*, **115**, 1693

[6] Disney, M.J. & Wall, J.V. 1977, *MNRAS*, **179**, 235

[7] Dwarakanath, K.S, & Owen, F.N. 1999, *ApJ*, **118**, 625

[8] Elfhag, T., Booth, R.S., Hoeglund, B., Johansson, L.E.B., & Sandqvist, A. 1996, *A&A Supl.*, **115**, 439

[9] Gavazzi, G., & Boselli, A. 1999, *A&A*, **343**, 93

[10] Helou, G., Khan, I.R., Malek, L., & Boehmer, L. 1988, *ApJS*, **68**, 151

[11] Hameed, S., & Devereux, N. 1999, *AJ*, **118**, 730

[12] Harwit, M., & Pacini, F. 1975, *ApJL*, **200**, 127

[13] Heisler, C.A., & Vader, J.P. 1995, *AJ*, **110**, 87

[14] Kennicutt, R.C. 1998, *ARA&A*, **36**, 189

[15] Menon T. K. 1995, *MNRAS*, **274**, 845

[16] Miller, N., & Owen, F.N 2001, *AJ*, *121*, 1903

[17] Neugebauer, G. et al. 1984, *ApJL*, **278**, 1

[18] Roussel, H., Helou, G., Beck, R., Condon, J.J., Bosma, A., Matthews, K., & Jarrett, T.H. 2003, *ApJ*, **593**, 733

[19] Roy, A.L.,Norris, R.P., Kesteven, M.J., Troup, E.R., & Reynolds, J. E. 1999, *MNRAS*, **301**, 1019

[20] Sanders, D.B., Scoville, N.Z., & Soifer, B.T. 1991, *ApJ*, **370**, 158

[21] Scodeggio, M., & Gavazzi, G. 1993, *ApJ*, **409**, 110

[22] Veilleux, S., & Rupke, D. S. 2002, ApJL, **565**, 63

[23] Willmer, C.N.A., Focardi, P., da Costa, L.N., & Pellegrini, P.S. 1989, *AJ*, **98**, 1531

[24] Yun, M.S., Reddy, N.A., & Condon, J.J. 2001, *ApJ*, **554**, 803

Appendix I

Multi-Frequency GMRT observations of the H II regions S 201, S 206, and S 209 : Galactic temperature gradient

Astronomy
&
Astrophysics

Multi-frequency GMRT observations of the HII regions S 201, S 206, and S 209

Galactic temperature gradient

A. Omar[1], J. N. Chengalur[2],[*], and D. Anish Roshi[3],[**]

[1] Raman Research Institute, C.V. Raman Avenue, Bangalore 560080, India
[2] National Centre for Radio Astrophysics, Post Bag 3, Ganeskhind, Pune 411007, India
[3] National Radio Astronomical Observatory, Green Bank, West Virginia, 24944-0002, USA

Abstract. We present radio continuum images of three Galactic H II regions, S 201, S 206, and S 209 near 232, 327, and 610 MHz using the Giant Meterwave Radio Telescope (GMRT). The GMRT has a mix of short and long baselines, therefore, even though the data have high spatial resolution, the maps are still sensitive to diffuse extended emission. We find that all three H II regions have bright cores surrounded by diffuse envelopes. We use the high resolution afforded by the data to estimate the electron temperatures and emission measures of the compact cores of these H II regions. Our estimates of electron temperatures are consistent with a linear increase of electron temperature with Galacto-centric distance for distances up to ~18 kpc (the distance to the most distant H II region in our sample).

Key words. ISM: H II regions – ISM: individual objects: S 201, S 206, S 209 – radio continuum: ISM

1. Introduction

A number of studies have indicated that the electron temperature T_e of H II regions increases with increasing Galacto-centric distance (e.g. Deharveng et al. 2000 and references therein). This effect is attributed to a decrease in heavy elements abundances with Galacto-centric distance. A low metal abundance leads to less effective cooling and consequently higher electron temperature. These studies are based either on estimates of T_e from radio recombination lines (RRLs) (which in turn depend on corrections for departures from local thermodynamic equilibrium (LTE) and for collisional broadening effects), or estimates based on line strengths of the forbidden line transitions of oxygen [O III]$\lambda\lambda$4363, 5007 (which are strongly dependent on temperature variations, if any, over the observed volume). Further, most of these studies are based on observations of H II regions with Galacto-centric distances $R_G \leq 15$ kpc with very few measurements of T_e beyond 15 kpc. Consequently most determinations of metalicities of the outer galaxy H II regions are based on values of T_e taken from an extrapolation of the observed gradient in temperature up to about 15 kpc (e.g., Deharveng et al. 2000). Since the O/H ratio (a commonly used indicator of metal abundance) depends sensitively on T_e,

metalicities of the outer galaxy H II regions are poorly constrained. In view of this, it is important to get independent estimates of the electron temperatures of H II regions in the outer galaxy.

An independent measurement of T_e can be obtained from radio continuum observations. The ionized material in H II regions emits radio continuum through free-free emission. At sufficiently low radio frequencies where the nebula is optically thick ($\tau \gg 1$), the emergent radiation is a black body spectrum, and therefore, the observed brightness temperature is equal to the electron temperature T_e. On the other hand, at sufficiently high radio frequencies, where the optical depth τ of thermal electrons is low ($\tau \ll 1$), the observed brightness is proportional to the emission measure of the nebula. Most of the available radio maps for H II regions are at high radio frequencies (i.e. above 1.4 GHz, e.g., Fich 1993; Balser et al. 1995). These maps show that H II regions often have a bright core with several knots surrounded by an extended envelop of diffuse emission. These core–envelope structures of H II regions imply that accurate measurement of T_e from low radio frequency observations requires high angular resolution, since, often only bright compact cores will be optically thick at frequencies of a few hundred MHz. This study presents an analysis of the low-frequency GMRT observations of three Galactic diffuse H II regions spanning Galacto-centric distances up to 18 kpc.

The GMRT is an ideal telescope for these observations since it operates at several low radio frequency bands, viz.,

Send offprint requests to: A. Omar, e-mail: aomar@rri.res.in
  [*] e-mail: chengalu@ncra.tifr.res.in
[**] e-mail: aroshi@gb.nrao.edu

150, 232, 327, 610, and 1420 MHz and also it has a hybrid configuration which makes it sensitive to both diffuse emission (on scales up to ~45′ at 232, 30′ at 327, and 17′ at 610 MHz) while also having the resolution (~15″ at 232, 10″ at 327, and 6″ at 610 MHz) to resolve the compact cores.

2. Observations

The observations were carried out during the period of August to December, 1999 at three frequency bands, viz., 232, 327, and 610 MHz. The GMRT has a "Y" shaped hybrid configuration of antennas with six antennas along each of the three arms and twelve antennas randomly placed in a compact arrangement near the centre of "Y" (for details, see Swarup et al. 1991). The compact array at the centre is about a kilometer across and is generally referred as the "central square". Baselines in the central square (shortest baseline ~100 m) provide sensitivity to diffuse large scale emission, while baselines involving arm antennas (longest baseline ~25 km) provide high angular resolution. The GMRT was in its commissioning phase during our observations, and due to various debugging and maintenance activities not all 30 antennas were available for observations. The observations were carried out with typically 20 to 25 antennas in different observing sessions.

The data were recorded in the default correlator mode which produces visibilities in 128 channels over a user selectable bandwidth in multiples of 2 starting from 62.5 kHz and up to 16 MHz. The observational parameters are summarized in Table 1. The observations near 610 and 327 MHz were made using the full 16 MHz bandwidth while observations near 232 MHz were made with a bandwidth of 2 MHz centered at a frequency around which least local interference has been detected in the past observations. The images at all frequencies are however made using data from only one channel which corresponds to a bandwidth of 125 kHz at 327 and 610 MHz, and 15.6 kHz at 232 MHz. This restriction was partly because of a crunch in disk storage at the time when these data were taken, and partly because dynamic range limitations at the GMRT at the time we took the data meant that the increase in bandwidth did not result in a proportionate increase in sensitivity. At each frequency band, we observed the source for about 8–10 hours, primarily in order to have a good (u, v) coverage.

For all the observations, the source 3C 48 was used as the primary flux calibrator. The flux density of 3C 48 at each frequency was estimated using the Baars et al. (1977) flux densities of standard VLA calibrators. The phase and amplitude gains of antennas were derived from observations of a secondary calibrator at intervals of 45 min. For observations on S 206 and S 209, 3C 119 was used as a secondary calibrator while 0107+562 was used as a secondary calibrator for observations on S 201. Both 3C 119 and 0107+562 are standard VLA calibrators. The fluxes of secondary calibrators were determined via boot-strapping the fluxes of the primary calibrator 3C 48.

The data were carefully checked for interference or other problems. At 232 and 327 MHz, a few short baselines were found to be corrupted, possibly by interference, and were removed. The data at 610 MHz were found to be free from any

interference. Data reduction was done in classic AIPS. The calibrated data were Fourier transformed using appropriate (u, v) ranges, tapers and weights to make different images, some of which are sensitive to large scale structures, and others which have the maximum possible angular resolution. These images were deconvolved using the "CLEAN" algorithm as implemented in AIPS task "IMAGR". The final gains of the antennas were fixed using several iterations of self-calibration.

The variations in system temperatures of GMRT antennas are currently not routinely monitored during observations. The system temperature at 610 MHz was measured both toward the absolute flux calibrator 3C 48 and the target source by firing the noise calibration diodes. For 327 and 232 MHz images, the system temperature toward 3C 48 and target source were obtained using interpolated values of sky temperature from 408 MHz all–sky map of Haslam et al. (1982). A correction factor equal to the ratio of the system temperature toward the target source and 3C 48 was applied in the deconvolved image. The deconvolved images were finally corrected for the primary beam attenuation, assuming a Gaussian shape for the primary beam. The half power points (HPBW) of the primary beam of GMRT antenna are estimated as 1.85, 1.35, and 0.72 degree for 232, 327 and 610 MHz respectively.

3. Results

Images of S 201 are shown in Figs. 1a–c. S 201, ($l = 138.48, b = 1.64$; also known as IC 1848), at a Galacto-centric distance of 10.5 ± 1 kpc, is believed to be excited due to a single star of spectral type O9.5 (Mampaso et al. 1989). High resolution (~5″) 15 GHz radio continuum image reveals a bright arc like core with multiple peaks of emission (Felli et al. 1987). The 616 MHz GMRT low resolution image (Fig. 1c) traces diffuse emission extending up to ~5′ which is consistent with the 1.4 GHz VLA image of Fich (1993). The high resolution 231 MHz GMRT image (Fig. 1b) shows the core to be a complex structure consisting of several unresolved compact sources. The diffuse nebulosity extending toward the west of the core in the 231 MHz image (Fig. 1b) is consistent with the 15 GHz radio image of Felli et al. (1987).

Images of S 206 are shown in Figs. 1d–f. S 206, ($l = 150.74, b = -0.75$; also known as NGC 1491), is an evolved H II region at a Galacto-centric distance of 11.1 kpc (Deharveng et al. 2000). The excitation is believed to be provided by a single O5 star (Crampton & Fisher 1974). The 5 GHz radio continuum image shows a classic blister type morphology (Fig. 4 in Deharveng et al. 1976) as described in Icke et al. (1980). Our high resolution images at 613 MHz (Fig. 1d), 236 MHz (Fig. 1e) as well as 328 MHz (not shown) show good correspondence to the 5 GHz image of Deharveng et al. (1976). The low resolution 328 MHz image (Fig. 1f) shows a large low intensity envelope surrounding the core emission.

Images of S 209 are shown in Figs. 1g–i. S 209 ($l = 151.6, b = -0.24$; also known as RAFGL 550) is one of the most distant ($R_G = 17.7$ kpc, Deharveng et al. 2000) Galactic H II region. Although the mean size of H II regions decreases with increasing Galacto-centric distance (Fich & Blitz 1984), S 209 is unusual in that it has a very large size (~50 pc)

Table 1. Observational details.

Field Centre RA (B1950)	Field Centre Dec (B1950)	Frequency (MHz)	Duration of observation (Hours)	Range of baselines (kλ)	rms noise in the image (mJy beam^{-1})
02^{h}59^{m}12^s	60°17′00″	231	8	0.05–15	2.5
		616	8	0.09–25	1.2
03^{h}59^{m}24^s	51°11′00″	236	9	0.05–18	7.4
		328	10	0.06–27	3.0
		613	10	0.09–49	1.2
04^{h}07^{m}18^s	51°02′00″	328	9	0.10–26	2.0
		613	10	0.10–50	1.0

Table 2. H II regions – results.

Name	α, δ (1950) h m s ° ′ ″	Frequency (MHz)	Flux (Jy)	Area (arcmin^2)	T_e (K)	EM (cm^{-6} pc)
S 201	02 59 20.1 60 16 10	231	0.78	16	7070 ± 1100	1.02(±0.05) × 10^5
		616	1.15	38		
S 206	03 59 24.0 51 11 00	236	16.3	329	8350 ± 1600	3.93(±0.40) × 10^5
		328	18.2	347		
		613	20.0	350		
S 209	04 07 20.1 51 02 30	236	13.4	267	10855 ± 3670	2.58(±0.29) × 10^5
		328	16.6	372		
		613	17.0	386		

for its Galacto-centric distance. The excitation is provided by a cluster of OB stars (Chini & Wink 1984). Our high resolution 613 MHz map (Fig. 1g) shows the core region to consist of an asymmetric, incomplete ring like structure. The high resolution image at 328 MHz (not shown here) is morphologically very similar to the 613 MHz image. The 236 MHz image (Fig. 1h) while showing overall similarity to the 613 MHz and 328 MHz maps, does show some difference in the core region. We are unsure why this should be so. The low resolution 613 MHz image (Fig. 1i) shows that this region too has an extremely large, low surface brightness envelope, which has also been seen at 2.7 GHz image of Walmsley et al. (1975).

4. Discussion

We use these low frequency images to estimate electron temperatures and emission measures of the compact cores of the H II regions. If we approximate these cores to be homogeneous and spherically symmetric, then the flux S is given by

$$S = 3.07 \times 10^{-2} T_e \nu^2 \Omega \left(1 - e^{-\tau(\nu)}\right) \qquad (1)$$

$$\tau(\nu) = 1.643a \times 10^5 \nu^{-2.1} EM\, T_e^{-1.35} \qquad (2)$$

(Mezger & Henderson 1967) where S is the integrated flux density in Jy, T_e is the electron temperature in Kelvin, ν is the frequency of observation in MHz, τ is the optical depth, Ω is the solid angle subtended by the source in steradian, (which in this case, since the cores are unresolved, is taken to be the synthesized beam size), and EM is the emission measure in cm^{-6} pc. The emission measure EM is defined as $\int n_e^2 \mathrm{d}l$; the integral

being taken along the line of sight and averaged over the beam. a is a correction factor which depends both upon the temperature and frequency. We have used an average value of a as 0.98 (using Table 6 of Mezger & Henderson 1967) for the frequency range 200–600 MHz and $T_e \sim 10\,000$ K. The H II region cores can be modeled by solving Eqs. (1) and (2) iteratively for different EM and T_e. The fitting procedure converges rapidly when observations at least two frequencies are available and the frequencies are such that the H II region is optically thick at one frequency and optically thin at the other.

We measured the peak flux densities of cores after convolving the images of a H II region at different frequencies to a common angular resolution (i.e. the source size Ω was taken to be $1.133 \times \theta_a \times \theta_b$, where θ_a and θ_b are the half power points of the common convolved beam). The best fit values for T_e and EM as obtained from the fitting procedure described above are listed in Table 2, and the observed and model fluxes are plotted in Fig. 2. The columns in Table 2 are as follows. Column 1: Name of the H II region, Col. 2: Coordinates (right ascension, declination) of the core for which the electron temperature has been measured, Col. 3: The frequency of observation, Col. 4: Integrated flux of the entire H II region, Col. 5: Area over which radio emission is detected, and over which the flux has been integrated to get the value listed in Col. 4, Col. 6: Estimated electron temperature of the core, Col. 7: Estimated emission measure of the core.

The electron temperature of S 201 is estimated to be 7070 ± 1100 K toward the peak radio emission. The earlier estimate for T_e toward S 201 was ~5000 K based on non-detection of [O III]$\lambda\lambda$4959, 5007 (Mampaso et al. 1989). The electron

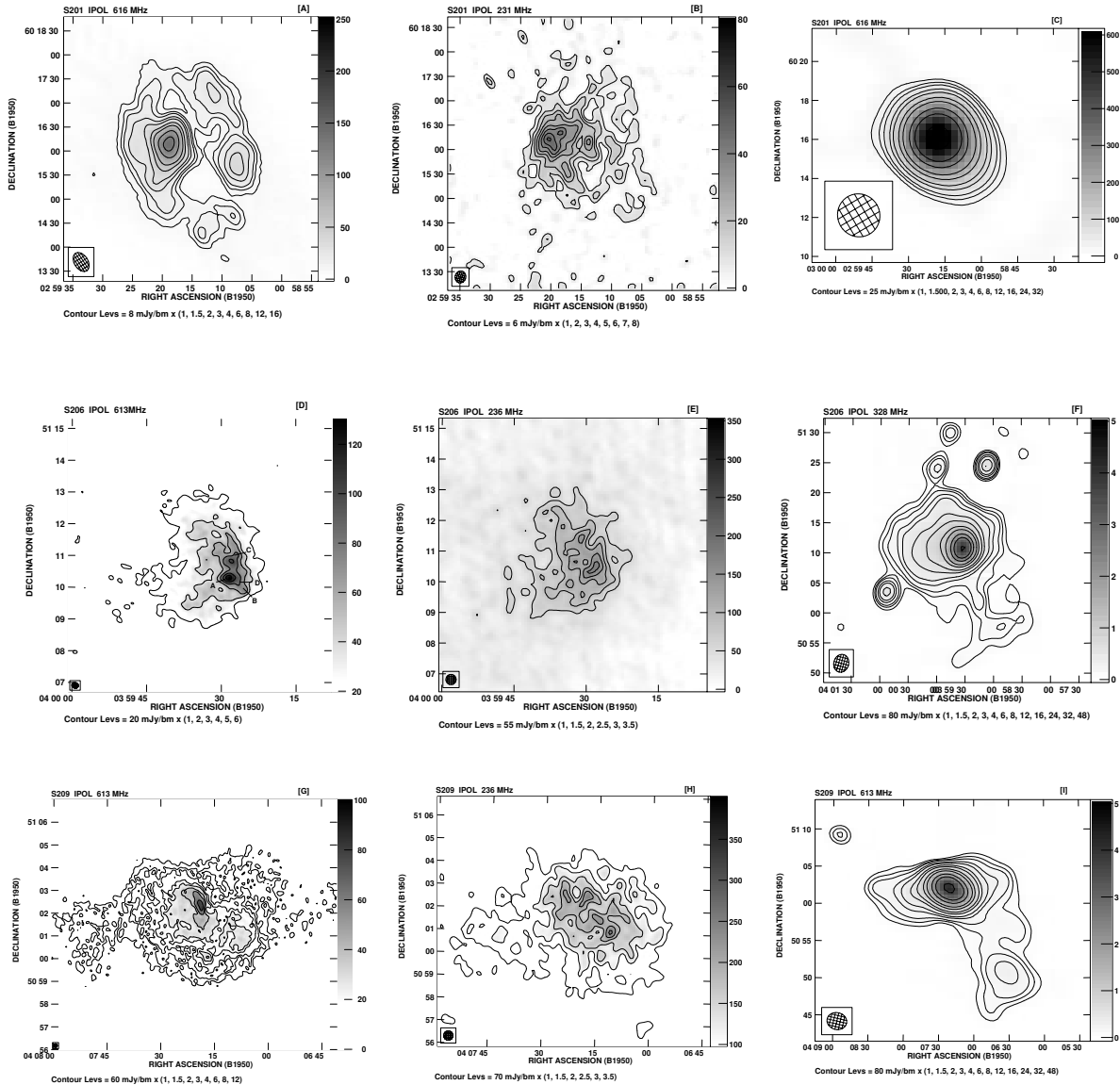230   A. Omar et al.: GMRT observations of H II regions

Fig. 1. a) S 201 at 616 MHz. The angular resolution is $26'' \times 17''$. **b)** S 201 at 231 MHz. The angular resolution is $15'' \times 13''$. **c)** S 201 at 616 MHz made using $u-v$ range 0–1 kλ only. The angular resolution is $133'' \times 129''$. **d)** S 206 at 613 MHz. The angular resolution is $13'' \times 11''$. The regions marked as A, B, C, & D are from the 5 GHz image of Deharveng et al. (1976). **e)** S 206 at 236 MHz. The angular resolution is $20'' \times 20''$. **f)** 328 MHz image of S 206 made using $u-v$ range 0–1 kλ only. The synthesized beam is $180'' \times 149''$. **g)** S 209 at 613 MHz. The angular resolution is $10'' \times 10''$. **h)** S 209 at 236 MHz. The angular resolution is $25'' \times 25''$. **i)** 613 MHz image of S 209 made using $u-v$ range only up to 1 kλ. The angular resolution is $160'' \times 136''$.

temperature of 8350 ± 1600 K, derived for the core of S 206 (knot–A in Fig. 1c) is in reasonable agreement with previous measurements, viz. 8400 ± 800 K obtained using the H94α recombination line by Carral et al. (1981), and 9118 K obtained from the [O III]$\lambda\lambda$4363, 5007 lines ratio (Deharveng et al. 2000). The emission measure is $3.93(\pm 0.40) \times 10^5$ cm^{-6} pc, consistent with the value obtained by Deharveng et al. (1976). For S 209, the electron temperature corresponding to the peak radio emission at 613 MHz is estimated to be 10 855 ± 3670 K, somewhat higher than the value of 8280 K obtained using the H137β recombination line by Churchwell et al. (1978) but in reasonable agreement with the estimate of 11 000 K which was

derived from H91α & H114β recombination lines (Balser et al. 1994).

Figure 3 is a plot of the electron temperature vs. Galacto-centric distance for the three H II regions studied in this paper. The solid line is the relationship obtained by Deharveng et al. (2000) from a sample of six H II regions spanning Galacto-centric distances from 6.6 to 14.8 kpc. The data for S 209 shows that this relationship appears to be valid even out to Galacto-centric distance of ~18 kpc.

If there are systematic radial temperature gradients within the cores of H II regions, the T_e estimated by various methods, viz., radio continuum, RRLs, and [O III]$\lambda\lambda$4363,

A. Omar et al.: GMRT observations of H II regions   231
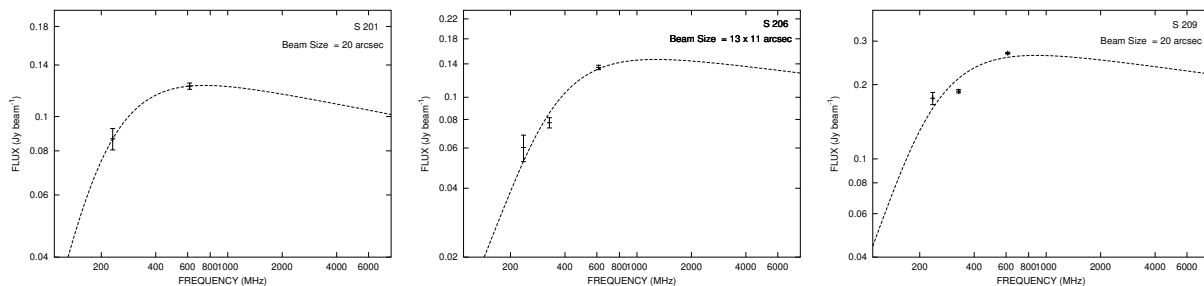

Fig. 2. Model and observed fluxes for the cores of the H II regions observed at the GMRT. The estimated emission measures and electron temperatures are listed in Table 2.

5007 lines ratio (all of which probe different physical regions) would be discordant. The radio continuum observations at low frequencies are more sensitive to outermost regions of the core of the nebula (due to the high optical depths at these frequencies). The temperature estimates from high frequency RRLs (which is where most of the observations exist) are weighted toward regions of low temperature. Finally, estimates of T_e from the [O III] lines ratio are expected to be weighted toward high temperature regions due to the high cooling rate provided by [O III] lines. Since, our estimates of T_e are in general consistent with those obtained from RRLs as well as from [O III] lines, any temperature gradients within the *cores* of these H II regions must be smaller than the combined uncertainties in these different T_e measurements. Similar concordance between T_e measured using these different methods have been obtained for W 51 (Subrahmanyan & Goss 1995) and M 17 (Subrahmanyan & Goss 1996; Wilson et al. 1997). Several authors have discussed the possibility of small scale temperature fluctuations in the cores of H II regions (Peimbert 1967; Rubin et al. 1998 and references therein), these cannot be ruled out based on our observations alone).

5. Conclusions

Three outer galaxy H II regions, S 201, S 206 and S 209 have been imaged at meter wavelengths using the GMRT. The images of these H II regions have been obtained at a resolution of less than a pc. This is the highest resolution achieved for any H II region at such low radio frequencies. All three H II regions show structures down to our resolution limit. The high resolution images near 610 MHz of these H II regions show a good correspondence with the radio continuum images at *cm* wavelengths. The low resolution radio images show that these H II regions are surrounded by large diffuse envelopes. The high resolution radio images have allowed us to get estimates of T_e of these H II regions. From these measurements we find that:

(1) the estimates of T_e are in general consistent with that obtained from RRLs and [O III]$\lambda\lambda$4363, 5007 line measurements, and

(2) the measured temperatures are consistent with a linear increase of T_e with Galacto-centric distance until $R_G \sim 18$ kpc.
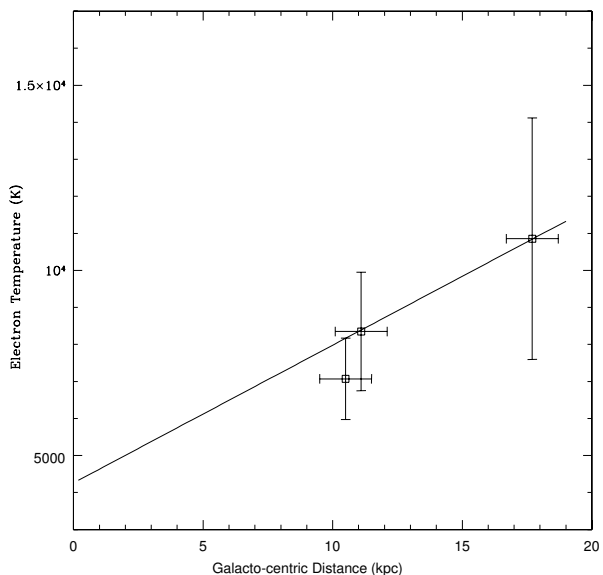
Fig. 3. The electron temperature vs. Galacto-centric distance for three H II regions studied in this paper. The solid line is the relationship derived by Deharveng et al. (2000) based on a sample of six H II regions spanning a Galacto-centric distance from 6.6 to 14.8 kpc.

References

Baars, J. W. M., Genzel, R., Pauliny-Toth, I. I. K., & Witzel, A. 1977, A&A, 61, 99

Balser, D. S., Bania, T. M., Brockway, C. J., Rood, R. T., & Wilson, T. L. 1994, ApJ, 430, 667

Balser, D. S., Bania, T. M., Rood, R. T., & Wilson, T. L. 1995, ApJS, 100, 371

Carral, P., Rodriguez, L. F., & Chaisson, E. J. 1981, A&A, 95, 388

Chini, R., & Wink, J. E. 1984, A&A, 139, L5

232   A. Omar et al.: GMRT observations of H II regions

Churchwell, E., Smith, L. F., Mathis, J., Mezger, P. G., & Huchtmeier, W. 1978, A&A, 70, 719

Crampton, D., & Fisher, W. A. 1974, Publ. Dominion Astrophys. Obs., 14(12)

Deharveng, L., Israel, F. P., & Maucherat, M. 1976, A&A, 48, 63

Deharveng, L., Pena, M., Caplan, J., & Costero, R. 2000, MNRAS, 311, 329

Felli, M., Hjellming, R. M., & Cesaroni, R. 1987, A&A, 182, 313

Fich, M. 1993, ApJS, 86, 475

Fich, M., & Blitz, L. 1984, ApJ, 279, 125

Haslam, C. G. T., Stoffel, H., Salter, C. J., & Wilson, W. E. 1982, A&AS, 47, 1

Icke, V., Gatley, I., & Israel, F. P. 1980, ApJ, 236, 808

Mampaso, A., Phillips, J. P., Vilchez, J. M., Pismis, P., & Riera, A. 1989, A&A, 220, 235

Mezger, P. G., & Henderson, A. P. 1967, ApJ, 147, 471

Peimbert, M. 1967, ApJ, 150, 825

Rubin, R. H., Martin, P. G., Dufour, R. J., et al. 1998, ApJ, 495, 891

Subrahmanyan, R., & Goss, W. M. 1995, MNRAS, 275, 755

Subrahmanyan, R., & Goss, W. M. 1996, MNRAS, 281, 239

Swarup, G., Ananthakrishnan, S., Kapahi, V. K., et al. 1991, Curr. Sci., 60, 95

Walmsley, C. M., Churchwell, E., Kazes, I., & Le Squeren, A. M. 1975, A&A, 41, 121

Wilson, T. L., Filges, L., Codella, C., Reich, W., & Reich, P. 1997, A&A, 327, 1177

Appendix II
VLA detection of OH absorption from the elliptical galaxy NGC 1052

Astronomy
&
Astrophysics

VLA detection of OH absorption from the elliptical galaxy NGC 1052

A. Omar[1], K. R. Anantharamaiah[1,*], M. Rupen[2], and J. Rigby[3]

[1] Raman Research Institute, C.V. Raman Avenue, Bangalore, 560 080, India
[2] National Radio Astronomy Observatory, Socorro, NM, USA
   e-mail: mrupen@aoc.nrao.edu
[3] Steward Observatory, University of Arizona, 933 N. Cherry Ave, Tucson, AZ 85721, USA
   e-mail: jrigby@as.arizona.edu

Abstract. VLA observations of OH absorption towards the elliptical galaxy NGC 1052 are presented. Both OH lines, at 1665 and 1667 MHz, were detected in absorption towards the center of NGC 1052. The hyperfine ratio of the two OH lines (τ_{1667}/τ_{1665}) is 2.6 ± 0.8 as compared to 1.8 expected for the excitation under LTE conditions for an optically thin cloud. The column density of OH is estimated to be $2.73\,(\pm 0.26) \times 10^{14}$ cm^{-2} assuming $T_{\rm ex} \sim 10$ K. The centers of both the OH lines are redshifted from the systemic velocity of the galaxy by ~ 173 km s^{-1}. The velocity of OH line coincides with the velocity corresponding to the strongest HI absorption. We suggest that OH absorption is arising from a molecular cloud falling towards the nucleus. The OH line, though narrower, is found to be within the much broader and smoother H$_2$O megamaser emission. The possible link between OH/HI and H$_2$O emission is discussed.

Key words. galaxies: active – galaxies: individual: NGC 1052 – galaxies: ISM – radio lines: galaxies

1. Introduction

The most extensive and conclusive confirmation for the presence of cold interstellar material in early-type galaxies came from observations of dust with the Infrared Astronomical Sattelite (IRAS) (Neugebauer 1984; Knapp et al. 1985; Knapp et al. 1989). Sensitive observations of HI (van Gorkom et al. 1989; Huchtmeier et al. 1995) have also shown that elliptical galaxies contain a significant amount of cold interstellar matter. The molecular contents of elliptical galaxies has been studied mainly through CO observations of infrared bright elliptical galaxies (Wang et al. 1992; Wiklind et al. 1995; Knapp & Rupen 1996). These observations resulted in the detection of molecular gas in several galaxies in emission and four galaxies in absorption, indicating that the overall detection rate of CO in elliptical galaxies is about 10–15%. The OH radical in absorption is also a good tracer of molecular gas in interstellar clouds (Liszt & Lucas 1996). Single dish OH surveys (Schmelz et al. 1986; Baan et al. 1992; Staveley-Smith et al. 1992; Darling & Giovanelli 2000) of several hundred galaxies of various types resulted in the detection of about 3 dozen galaxies, of which none was an elliptical.

NGC 1052, a moderately luminous ($L_{\rm b} = 1.6 \times 10^{10}\ L_{\odot}$) elliptical galaxy of type E4, is a member of a small group in the Cetus–I cloud. There are several estimates of the velocity for this system in the literature, which differ from each other by a few tens of km s^{-1}. We adopt $V_{\rm hel} = 1474 \pm 10$ km s^{-1}, estimated from the optical emission lines (de Vaucouleurs 1991), which implies that NGC 1052 is at a distance of 21 Mpc (assuming $H_0 = 70$ km s^{-1} Mpc^{-1} and $q_0 = 0$). It is classified as a LINER (Fosbury et al. 1978; Ho et al. 1997) and is known for its several water megamasers (Braatz et al. 1996; Claussen et al. 1998). HI absorptions, redshifted from the systemic velocity, were detected at 1486, 1523 and 1646 km s^{-1} against the nuclear continuum source (van Gorkom et al. 1986). NGC 1052 was reported to have CO emission as well as absorption by Wang et al. (1992), but later observations by Wiklind et al. (1995) failed to confirm those detections. More recently, Knapp & Rupen (1996) have reported a possible CO absorption from NGC 1052 near 1622 km s^{-1}. Since the reported CO detections are quite noisy, it remains uncertain whether NGC 1052 has a molecular component associated with the HI (21 cm) absorption.

Here we report the first detection of 1665 and 1667 MHz OH absorption in NGC 1052. The next section describes the observational details and results. Subsequent sections compare these results with observations at

---

L30   A. Omar et al.: OH absorption from NGC 1052

Table 1. Observation parameters.

Parameter	Value
Date of observation	1998 Sep. 03
RA, Dec (J2000.0)	02 41 04.79, –08 15 20.75
Observing duration (hrs)	5
Range of baselines (km)	0.1–11 (B config)
Observing frequencies (MHz)(IF1,IF2)	1656.50, 1658.30
Bandwidth per IF (MHz)	1.562
Number of spectral channels	64
Polarizations	RCP & LCP
Synthesised beam (Natural Weight)	6.4″ × 4.3″, PA = 9.7°
Velocity resolution	4.4 km s^{-1}
Frequency resolution (kHz/channel)	24.4
Amplitude calibrator	0137+331 (3C 48)
Phase calibrator	0240–231
Bandpass calibrator	0319+415 (3C 84)
rms noise per channel (mJy beam^{-1})	0.7

optical, X-ray, and other wave bands, and discuss some of the implications.

2. Observations and results

NGC 1052 was observed in the B configuration of the VLA, which has interferometric baselines ranging from 100 m to 11 km. Data were recorded in the 4IF correlator mode, recording 1.5625 MHz in each of the two circular polarizations for two frequency bands, one centered at 1656.5 and other at 1658.3 MHz. The details of the observations are listed in Table 1. The data were reduced in AIPS using standard calibration and imaging methods. The amplitude, phase and frequency response of the antennas were calibrated separately for each IF. The phase and amplitude gains of the antennas were derived from observations of the standard VLA calibrator 0240–231 at intervals of 30 min. The flux scale was set using Baars et al. (1977) flux density of the standard VLA calibrator 3C 48. A combined bandpass spectrum was generated using all the data taken on the amplitude and phase calibrators as well as on the strong radio source 0319+415 (3C 84). A continuum data set was formed by averaging the calibrated visibility data of 50 line-free channels. The continuum data set was self-calibrated and the resulting antenna gain corrections were applied to every spectral channel separately. The continuum emission common to all channels was removed using the task "UVLIN" inside AIPS. Continuum–free images for all channels were made and the source region was searched for absorption. Both 1665 and 1667 MHz lines were detected, in each of the two circular polarizations. Although, a part of the band centered at 1656.5 MHz was affected by interference, the detected 1665 MHz line was outside the affected region.

The core/jet morphology in the continuum image of NGC 1052 is in accordance with the previous observations by Jones et al. (1984). The peak continuum flux density of the core is ∼1.14 Jy. The total flux density including contributions from the two radio lobes is ∼1.23 Jy. The continuum image (Fig. 1) shows that the radio axis is at a position angle (E to N) of 103°. The two radio lobes are

asymmetrically located about the radio nucleus, being 14″ to the east and 8″ to the west. The continuum nucleus and the line absorption are unresolved with the synthesised beam (6.4″ × 4.3″, PA = 9.7°). Both 1665 and 1667 MHz lines are detected at a redshifted velocity of ∼173 km s^{-1} with respect to the systemic velocity of the galaxy. The column density of OH can be estimated from

$$N_{\mathrm{OH}} = 2.35 \times 10^{14} \, T_{\mathrm{ex}} \int \tau_{1667} \, \mathrm{d}V \, \mathrm{cm}^{-2} \qquad (1)$$

(Dickey et al. 1981; Liszt & Lucas 1996) where T_{ex} is the excitation temperature in Kelvins, τ_{1667} is the optical depth of the 1667 MHz line and V is the velocity in km s^{-1}; for NGC 1052, above equation gives an OH column density of $2.73 \, (\pm 0.26) \times 10^{14} \, (T_{\mathrm{ex}}/10)$ cm^{-2} towards the center. For the two lobes, we estimate an average 3σ upper limit of OH absorption as ∼0.10. This upper limit implies that 0.6% absorption seen towards the nucleus is undetectable from either of the lobes even if absorbing gas covers the entire continuum source.

The AIPS gaussian fitting routine "SLFIT" was used to derive the line parameters. The peak optical depth of the 1667 MHz line is $5.8 \, (\pm 0.2) \times 10^{-3}$ and that of the 1665 MHz line is $2.9 \, (\pm 0.1) \times 10^{-3}$. The *FWHM* of 1667 and 1665 MHz lines are 18.8 ± 1.3 and 14.5 ± 2.6 km s^{-1} respectively. Given the uncertainty in the overall shape of the 1665 MHz line due to low optical depth, profiles of the 1665 and 1667 MHz lines can be considered similar. The ratio of the integrated optical depth is 2.6 ± 0.8 which is marginally higher than that expected (viz. 1–1.8) for excitation in thermal equillibrium. The mean value of 1667 to 1665 MHz line ratio is about 1.6 for galactic diffuse clouds (Dickey et al. 1981).

3. Discussion

3.1. Link with HI and X-ray absorbing column

HI components in NGC 1052 have been seen in absorption at 1486, 1523 and 1646 km s^{-1}, which are redshifted from the systemic velocity (van Gorkom et al. 1986). The $N(\mathrm{HI})/T_{\mathrm{ex}}$ values of three components are 0.6×10^{18}, 1.0×10^{18} and 1.4×10^{18} cm^{-2} respectively. The strongest absorption ($\tau \sim 0.02$) is at 1646 km s^{-1} with a *FWHM* of about 35 km s^{-1}. Due to the similarity in the velocity of OH absorption with the highest redshifted component of HI absorption, it is reasonable to associate this HI component with the OH detected in these observations. It is interesting that the velocity of OH absorption matches very well with the strongest HI absorption component at 1646 km s^{-1} even after a difference of about 16 years in the observations. The stability of OH/HI line suggests that the absorbing cloud covers a substantial fraction of the milliarcsec VLBI core in which most of the radio emission lies (Jones et al. 1984; Kameno et al. 2001). The integrated optical depth ratio of HI to OH is ∼6, which is in accordance with the values obtained for the galactic diffuse clouds (Dickey et al. 1981). The linewidth ratio of HI
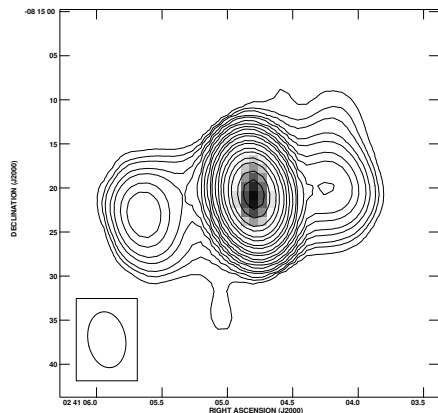
Fig. 1. The radio continuum image of NGC 1052 drawn as contours with levels of 1.8 mJy beam^{-1} $\times$ (1, 1.5, 2, 3, 4, 6, 8, 12, 16, 24, 32, 48, 64, 96, 128, 192, 256, 384, 512). The peak flux density in the contour image is 1.14 Jy beam^{-1}. The peak flux densities of the E and W lobes are 22.3 and 19.4 mJy beam^{-1} respectively. The grey scale represents the velocity–integrated optical depth of the 1667 MHz OH absorption. The synthesised beam depicted in the bottom left corner is $6.4'' \times 4.3''$, PA $= 9.7°$.
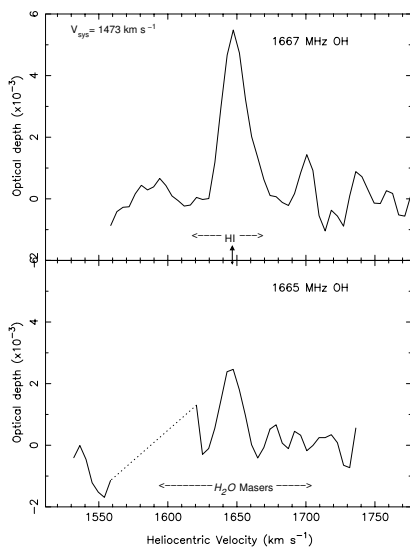
Fig. 2. A plot of the optical depth of 1667 and 1665 MHz absorption lines towards the nucleus of NGC 1052. The spectrum has been Hanning smoothed offline using a window of 3 adjacent channels. The figure displays the entire velocity coverage by VLA observations. The region marked by dashed lines in 1665 MHz spectrum was affected by interference. The velocity range over which HI absorption and H_2O masers are observed are indicated in the top and bottom frames respectively. The systemic velocity is indicated on top left corner of the upper frame.

to OH is $\sim$2, which suggests that the excitation of OH is restricted to some preferred regions inside the cloud. If redshifted absorption is considered as an evidence of infall of gas to the nucleus, where a small fraction of the gaseous mass is converted to luminosity, then, the association of a large amount of molecular gas with the neutral gas will imply a lower efficiency of the central engine in converting mass to luminosity. The observed line widths (*FWHM*) viz. $\sim$18 km s^{-1} of the two OH absorption is considerably higher than would be expected ($\sim$1 km s^{-1}) from purely thermal motions, assuming the gas temperature is at most a few tens of K. However, if the gas is very close (within few pc) to the nucleus, some kinematical effects will tend to broaden the observed absorption line e.g., turbulence may set up to overcome the gravitational collapse against the nucleus. If the gas is in a disk, then, a velocity gradient along the disk, as seen in some megamaser galaxies (e.g. Hagiwara et al. 2000), can explain the observed line width of the OH absorption. On the other hand, if the observed dispersion is considered due to conglomerate of individual clouds in virial equilibrium, a binding mass will be about 10^6 $M_\odot$, a value close to that seen in some giant molecular clouds (GMCs) of our galaxy. The typical velocity width of such GMCs has been estimated close to 10 km s^{-1} (Stark & Blitz 1978).

The gas is expected to be much hotter in the vicinity of an AGN due to enhanced Lyα pumping which in turn will increase the $T_{\rm ex}$ to a few thousand kelvin. Assuming, $T_{\rm ex} \sim 1000$ K, the predicted total N(HI) will be 2.0×10^{21} cm^{-2} including all three HI components. For the detected OH component, taking the relative abundance ratio of OH/H_2 = 1×10^{-7} (Guèlin 1985; Liszt & Lucas 1999), the implied column density of H_2 is 2.73×10^{21} ($T_{\rm ex}/10$) cm^{-2}. The implied CO column density is about 5.5×10^{14} cm^{-2}, which is about 10 times higher than predicted from CO observations. In comparison, X-ray observations indicate a hydrogen column density greater than 1×10^{23} cm^{-2} (Weaver et al. 1999), which is significantly higher than the total hydrogen column estimated via radio observations (HI & OH). This excess column density inferred from X-ray data has been seen in many active galaxies, and, was explained due to excess absorption by a combination of dust and partially ionized gas (Gallimore et al. 1999). It should be noted here that since HI and OH absorptions are spatially unresolved, the estimated values of OH and HI column densities are only a lower limit. Also, X-ray absorption is arising towards the nucleus which is free-free absorbed at wavelengths corresponding to the HI and OH absorptions (Kameno et al. 2001), therefore, radio observations are sampling off nuclear gas which may be of different composition than the gas probed via X-ray observations.

3.2. Link with H_2O megamasers?

It is very surprising that the OH absorption, though narrower than the water maser emission, is coincident

Letter to the Editor

with the velocity centroid of the 22 GHz H_2O masers. NGC 1052 is the only known elliptical galaxy having H_2O megamaser emission. The megamasers and their link with AGNs are generally understood in terms of obscuring torus models. The link is thought to be a consequence of irradiation of the inner face of the torus by hard X-rays from the nuclear continuum source, which enhances the water abundance within a molecular layer at a temperature of 400–1000 K (Neufeld et al. 1994). H_2O megamasers of NGC 1052 are unusual in showing a relatively smooth profile which moves in velocity over time by about 70 km s^{-1} on a time scale of a year (Braatz et al. 1996). Water masers in NGC 1052 are distributed along the jet rather than perpendicular to it (Claussen et al. 1998) unlike in NGC 4258 in which water masers are originating in a torus (see Miyoshi et al. 1995). Claussen et al. (1998) suggested that these masers are excited by shocks in to circumnuclear molecular cloud, or alternatively, amplifying radio continuum emission of the jet by foreground molecular clouds. It should be noted that the shocks can also enhance the abundance of OH by dissociation of H_2O before the gas is cooled down below 50 K (Wardle 1999), however, the observed column density of OH is one order of magnitude less than that predicted. A drift in the velocity of maser feature was considered as a consequence of the moving jet which will illuminate different parts of the foreground H_2O masing cloud. Efficient maser emission will take place at total column density (N_H) below the quenching density which is estimated as $10^{25}-10^{27}$ cm^{-2} for NGC 1052 (see Weaver et al. 1999). This upper limit on column density is well above than that predicted from our observations. However, it is not clear how HI/OH are quite stable over a long period of time while H_2O emission changes substantially over a short time scale. Further simultaneous observations of HI, OH and H_2O masers are required to make a connection between molecular gas traced by OH absorption and H_2O masing gas.

4. Summary

These VLA observations have resulted in the first detection of OH absorption in an elliptical galaxy. Both, 1665 and 1667 MHz OH absorption, were detected from the elliptical galaxy NGC 1052. The linewidths of both the OH lines are significantly large as compared to that expected for a cloud in thermal conditions at few tens of K. The gas is predicted to be close to the nucleus. A remarkable coincidence of velocity is found with the strongest and redshifted HI absorption and H_2O emission, however link to the megamaser emission is still not understood. Based on the abundance ratio of OH/H_2 as 1×10^{-7}, it is predicted that the column density of molecular gas in NGC 1052 is comparable to HI. Higher angular and spectral resolution observations would be usefull for detail kinematics of the OH absorption while simultaneous observations of H_2O and HI/OH observations would be neccessary to understand the link between masing gas and molecular gas traced by OH absorption.

References

Baan, W. A., Haschick, A. D., & Henkel, C. 1992, AJ, 103, 728
Baars, J. W. M., Genzel, R., Pauliny-Toth, I. I. K., & Witzel, A. 1977, A&A, 61, 99
Braatz, J. A., Wilson, A. S., & Henkel, C. 1996, ApJ, 106, 51
Claussen, M. J., Diamond, P. J., Braatz, J. A., Wilson, A. S., & Henkel, C. 1998, ApJ, 500, L129
Darling, J., & Giovanelli, R. 2000, AJ, 119, 3003
de Vaucouleurs, G., de Vaucouleurs, A., Corwin, H. G. Jr., et al. 1995, in Third Reference Catalogue of bright galaxies, version 3.9
Dickey, J. M., Crovisier, J., & Kazès, I. 1981, A&A, 98, 271
Fosbury, R. A. E., Mebold, U., Goss, W. M., & Dopita, M. A. 1978, MNRAS, 183, 549
Gallimore, J. F., Baum, S. A., O'Dea, C. P., Pedlar, A., & Brinks, E. 1999, ApJ, 524, 684
Guèlin, M. 1985, in Molecular Astrophysics, ed. by W. F. Diercksen, W. F. Huebner, & P. W. Langhoff (Reidel), 23
Hagiwara, Y., Diamond, P. J., Nakai, N., & Kawabe 2000, A&A, 360, 49
Ho, L. C., Filippenko, A. V., & Sargent, W. L. W. 1997, ApJS, 112, 315
Huchtmeier, W. K., Sage, L. J., & Henkel, C. 1995, A&A, 300, 675
Jones, D. L., Wrobel, J. M., & Shaffer, D. B. 1984, ApJ, 276, 480
Kameno, S., Sawada-Satoh, S., Inoue, M., Zhi-Qiang, S., & Kiyoaki, W. 2001, PASJ, 53, 169
Kazes, L., & Dickey, J. M. 1985, A&A, 152, 9
Knapp, G. R., Guhathakurta, P., & Kim, D. W. 1989, ApJS, 70, 329
Knapp, G. R., & Rupen, M. P. 1996, ApJ, 460, 271
Knapp, G. R., Turner, E. L., & Cunniffe, P. E. 1985, AJ, 90, 454
Liszt, H., & Lucas, R. 1996, A&A, 314, 917
Liszt, H., & Lucas, R. 1999, Highely Redshift Radio Lines, ed. by Carilli et al., ASP Conf. Ser., 156, 188
Miyoshi, M., Moran, M., Herrnstein, J., et al. 1995, Nature, 373, 127
Neufeld, D. A., Maloney, P. R., & Conger, S. 1994, ApJ, 436, L127
Neugebauer, G. 1984, ApJ, 278, L1
Schmelz, J. T., Baan, W. A., Haschick, A. D., & Eder, J. 1986, AJ, 92, 1291
Stark, A. A., & Blitz, L. 1978, ApJ, 225, L15
Staveley-Smith, L., Norris, R. P., Chapman, J. M., et al. 1992, MNRAS, 258, 725
van Gorkom, J. H., Knapp, J. H., Ekers, S. M., et al. 1989, AJ, 97, 708
van Gorkom, J. H., Knapp, G. R., Raimond, E., Faber, S. M., & Gallagher, J. S. 1986, AJ, 91, 791
Wang, Z., Kenney, J. D. P., & Ishizuki, S. 1992, AJ, 104, 2097
Wardle, M. 1999, ApJ, 525, L101
Weaver, K. A., Wilson, A. S., Henkel, C., & Braatz, J. A. 1999, ApJ, 520, 130
Wiklind, T., Combes, F., & Henkel, C. 1995, A&A, 297, 643

Appendix III

GMRT and VLA observations of H I and OH from the Seyfert galaxy
Mrk 1

Astronomy
&
Astrophysics

GMRT and VLA observations of H I and OH from the Seyfert galaxy Mrk 1

A. Omar[1], K. S. Dwarakanath[1,2,*], M. Rupen[2,**], and K. R. Anantharamaiah[1,***]

[1] Raman Research Institute, C.V. Raman Avenue, Bangalore, 560 080, India
[2] National Radio Astronomy Observatory, PO Box O, Socorro, NM 87801, USA

Abstract. We present Giant Meterwave Radio Telescope (GMRT) observations of the H I 21 cm line and Very Large Array (VLA) observations of the OH 18 cm line from the Seyfert 2 galaxy Mrk 1. H I emission is detected from both Mrk 1 and its companion NGC 451. The H I emission morphology and the velocity field of Mrk 1 are disturbed. We speculate that the nuclear activities of Mrk 1 are triggered by tidal interactions. We estimate the H I masses of Mrk 1 and NGC 451 to be $8.0(\pm0.6) \times 10^8 \, M_\odot$ and $1.3(\pm0.1) \times 10^9 \, M_\odot$ respectively. We have also detected the H I 21 cm line and the OH 18 cm line in absorption toward the nucleus of Mrk 1 at a blueshifted velocity with respect to its systemic velocity indicating an outflow of atomic and molecular gas. Two OH lines, at 1665 and 1667 MHz, are detected. Each of the profiles of the H I and OH absorption consists of two components that are separated by $\sim$125 km s^{-1}. Gaussian fitting gave dispersions of $\sim$44 km s^{-1} for both the components of the H I absorption. The profile of the OH absorption is qualitatively similar to that of the H I absorption. Both components of the OH absorption are thermally excited. The peak optical depths of the two components of the H I absorption are $(7.3 \pm 0.4) \times 10^{-2}$ and $(3.2 \pm 0.4) \times 10^{-2}$. The corresponding peak optical depths of the 1667 MHz OH absorption are $(2.3 \pm 0.3) \times 10^{-2}$ and $(1.1 \pm 0.3) \times 10^{-2}$. The higher velocity components of the H I and OH (1667 MHz) absorption lines are blueshifted from the [O III]λ5007, [O I]λ6300, and the systemic velocity by $\sim$100 km s^{-1}, but are consistent with the [O II]λ3727 velocity. We explain these velocity discrepancies as due to shock ionization of a region which is pushed forward due to shocks in front of the radio nucleus thereby giving apparent blueshift to H I, OH, and [O II] velocities. The optical depth ratios $\tau_{\rm H I}/\tau_{\rm OH}^{1667}$ of both the components of the H I and OH absorption are $\sim$3, indicating their origin in dense molecular clouds. Using OH/A_v values for the Galactic molecular clouds, we obtain $9 < A_v < 90$ toward the line of sight of Mrk 1.

Key words. galaxies: active – galaxies: interactions – galaxies: individual: Mrk 1, NGC 451 – galaxies: ISM

1. Introduction

Both the AGN and the nuclear starburst activities in galaxies that require inflow of material toward the centre either to fuel the central black hole or to cause rapid burst of nuclear star formation can be accomplished by tidal interactions (Hernquist & Mihos 1995). It is not clear, however, in the case of Seyfert galaxies whether nuclear activities in these low luminosity active galactic nuclei (AGN) are due to interactions as found in QSOs, radio galaxies, and BL Lacs (see De Robertis et al. 1998 for a review on the subject). It is generally accepted that interactions leading to mergers (bound interactions) may play a more significant role in triggering nuclear activities than unbound or hyperbolic encounters (De Robertis et al. 1998). Interactions can be effectively traced via H I 21 cm line emission from galaxies as H I disks often extend well beyond the optical radii of galaxies where the disks respond quickly to gravitational perturbations.

Send offprint requests to: A. Omar,
e-mail: aomar@rri.res.in
* e-mail: dwaraka@rri.res.in
** e-mail: mrupen@aoc.nrao.edu
*** Deceased.

H I emission studies may be particularly useful since most often the H I morphology provides evidence of interactions which are undetectable at optical wavelengths (e.g., Simkin et al. 1987).

H I in absorption can trace kinematics and distribution of atomic gas near the centres of active galaxies on the size scales of their background radio sources. The advantage of absorption studies is that they can detect relatively small quantities of gas irrespective of the redshift of the object. Recently, Gallimore et al. (1999) found H I rich absorbing disks on the scales of a few hundred parsecs in several Seyfert galaxies. As a result of intense nuclear activities, gas in the central regions of active galaxies may be perturbed due to interactions of the radio plasma with the surrounding ISM which may result in bulk outflows of material (e.g., Tadhunter et al. 2001; Morganti et al. 1998). The molecular gas near the centres of active galaxies can be traced via the 18 cm OH line in absorption. The 18 cm OH absorption line is sensitive to molecular gas in both the diffuse ISM and in the dark clouds with the OH to H_2 ratio being almost constant over a large range of Galactic clouds (Liszt & Lucas 1996). Studies have shown that chances of detecting OH absorption are higher in infrared luminous galaxies (Schmelz et al. 1986).

In this paper, we present synthesis observations of the H I 21 cm line obtained with the GMRT and the OH 18 cm line obtained with the VLA of the infrared luminous active galaxy Mrk 1 and its companion NGC 451. The global properties of Mrk 1 are summarized in the next section. The details of observations and data analyses are given in Sect. 3. The results are presented in Sect. 4. Section 5 discusses the radio continuum properties, H I emission, and H I and OH absorption. The conclusions are in the last section.

2. Global properties of Mrk 1

The global properties of Mrk 1 are listed in Table 1. Mrk 1 (NGC 449; B_T^0 = 14.53) is a member of a poor group (WBL 035) at a redshift of 0.017 (White et al. 1999). The other two members of this group viz., NGC 447 and NGC 451, are at projected separations from Mrk 1 of ~38 kpc and ~130 kpc respectively. Mrk 1 is classified as a SB 0/a galaxy with a Seyfert type 2 nucleus (Markarian et al. 1989) with no signatures of interactions in the optical images. Mrk 1 is also a luminous Infrared galaxy (L_{FIR} = 1.7×10^{10} $L_\odot$), indicating a high rate of star formation. Mrk 1 is one among 16 galaxies detected in the 22 GHz water megamaser emission in a sample of 354 active galaxies (Braatz et al. 1994). The nuclear optical spectrum of Mrk 1 studied by Koski (1978) and Weedman et al. (1968) shows strong emission lines typical of an active galaxy photo-ionized by hard continuum. The broad lines indicative of a hidden Seyfert nucleus are not found either in the infrared (Veilleux et al. 1997) or in the polarized light (Kay et al. 1994). High dispersion spectroscopic observation of the [O III]λ5007 line by Bergeron & Durret (1987) shows a distinct blue asymmetry indicative of an outflow of gas. Keel (1996) suggested that the nuclear activities of Mrk 1 are due to an ongoing interaction with the nearby galaxy NGC 451.

The radio continuum emission from Mrk 1 is known to have a steep spectrum with a spectral index α ($S \propto \nu^{-\alpha}$) of 0.8 (Dickinson et al. 1976). The 1.6 GHz EVN image (resolution ~30 pc) of Kukula et al. (1999) shows that the nuclear emission to consists of an unresolved core surrounded by a weak diffuse emission with a total flux density of 34 mJy. The NVSS flux density at 1.4 GHz is 75.4 mJy.

The Arecibo observations by Hutchings (1989) detected H I emission and blueshifted H I absorption from Mrk 1. This single dish spectrum could not separate H I emission from Mrk 1 and NGC 451. Observations with the Nobeyama Radio Telescope detected CO (J = 1–0) emission with a total flux integral of 11.5 ± 1.6 K km s^{-1} from the central 5 kpc region of Mrk 1 (Vila-Vilaro et al. 1998). The search for the 18 cm OH absorption by Schmelz et al. (1986) with the Arecibo reflector resulted in a non-detection with an rms sensitivity to an optical depth of 0.02.

3. Observations and data analyses

3.1. The GMRT observations

The GMRT observations of Mrk 1 were carried out in October, 2000. A summary of the main observational parameters are

given in Table 2. At the time of the observations, the GMRT was not fully operational and hence not all 30 antennas were available for observations at any given time. Two runs of observations with 18–20 antennas, each with a field of view (*FWHM*) 24′ centered on Mrk 1, were carried out on two different days. The GMRT has a mix of both short and long baselines (see Swarup et al. 1991 for more details), making it sensitive to diffuse emission of an extent of as much as 7′ while having a maximum resolution of ~3″ at 1.4 GHz. The GMRT uses a 30-station FX correlator which produces complex visibilities over 128 spectral channels in each of the two polarizations. The bandwidth can be selected in multiples of 2 between 62.5 kHz and 16 MHz. These observations were carried out with a bandwidth of 8 MHz centered at 1395.0 MHz, which covered H I velocities in the range 3730–5460 km s^{-1} with a velocity resolution of ~14 km s^{-1}.

The complex gains of the antennas were determined every 30 min using observations of an unresolved nearby (~4.5°) source (3C 48) for 5 min. 3C 48 was also used for the flux and the bandpass calibrations. The data were reduced, following standard calibration and imaging methods, using the Astronomical Image Processing Software (AIPS) developed by the NRAO. The data were calibrated for the amplitude, phase, and frequency response for all antennas separately for each polarization. The flux density of 3C 48 was estimated to be 16.228 Jy at the observing frequency using the 1999.2 VLA flux densities of the standard VLA flux calibrators and the formula given in the AIPS task "SETJY". Due to the close proximity of 3C 48 to Mrk 1 and based on some previous test experiments, we expect that the flux calibration is accurate to within 5%.

A continuum data set was formed by averaging 80 line-free channels. The data were self calibrated in both phase and amplitude. The resulting antenna gain corrections were applied to all channels. The continuum images were made using the self-calibrated averaged data from the line-free channels. The continuum flux density from each individual channel was subtracted in the (u, v) dataset by a linear fit to the visibilities in the line-free channels. Since these observations were also sensitive to H I emission, the data points were "natural-weighted" to enhance sensitivity to extended features. The resulting spectral cubes were CLEANed for signals greater than 4 times the rms noise in the channel images. The cube was blanked for emission below a level of 1.5σ in the images after applying a Hanning smoothing of three velocity channels and Gaussian smoothing of five pixels (pixel size = 6″) in the spatial coordinates. The zeroth and first order moment maps were generated from the blanked channel images containing H I emission and two additional channels on both the sides.

3.2. The VLA observations

The VLA "B" configuration observations were carried out in March, 2001. The observational parameters are summarized in Table 2. The data were recorded in the 1A correlator mode with a total bandwidth of 6.25 MHz divided into 128 channels. These observations covered a velocity range

Table 1. Global properties of Mrk 1.

Parameter	Value	Reference
Right Ascension (J2000)	$01^h 16^m 07\overset{s}{.}1$	1
Declination (J2000)	$33°05'22''$	1
Distance (Mpc)	68	2
Hubble type	SB 0/a	1
Seyfert type	2	1
Inclination	$45°$	3
Optical diameter (kpc)	9.0×5.3	1
Corrected blue magnitude B_T^o	14.53	4
Total blue luminosity ($L_\odot$)	1.1×10^{10}	
Total H I mass ($M_\odot$)	8.0×10^8	5
H I mass to blue luminosity ratio ($M_\odot/L_\odot$)	0.07	5
Total FIR luminosity ($L_\odot$)	1.7×10^{10}	6
1.4 GHz radio luminosity (W Hz^{-1})	4.2×10^{22}	5
Spectral index ($S \propto \nu^{-\alpha}$) (2.7 GHz–10.5 GHz)	0.8	7
X-ray luminosity (erg s^{-1})	$<10^{41}$	8
Systemic velocity (km s^{-1})	4780 ± 2	9
[O III] λ 5007 velocity (km s^{-1})	4822 ± 25	10
[O II] λ 3727 velocity (km s^{-1})	4697 ± 25	10
[O I] λ 6300 velocity (km s^{-1})	4817 ± 25	10
Mean velocity of H I emission (km s^{-1})	4780	5
H$_2$O maser velocity (km s^{-1})	4868 ± 1	3
Mean velocity of CO emission (km s^{-1})	4850	11

Notes: $H_0 = 75$ km s^{-1} Mpc^{-1}. The velocity definition is optical and Helio-centric.
1: Markarian et al. (1989); 2: White et al. (1999); 3 Braatz et al. (1997); 4: NED (NASA Extragalactic Database); 5: This paper; 6: IRAS faint source catalog, (1990); 7: Dickinson et al. (1976); 8: Fabbiano et al. (1992); 9: Keel (1996); 10: De Robertis & Shaw (1990) 11: Vila-Vilaro et al. (1998).

Table 2. Observational parameters.

Parameter	GMRT	VLA
Dates of Observations	2000 Oct. 25, 28	2001 Mar. 26, 27
Pointing centre (RA J2000.0)	$01^h 16^m 07\overset{s}{.}25$	$01^h 16^m 07\overset{s}{.}25$
Pointing centre (Dec J2000.0)	$+33°05'22''\!.2$	$+33°05'22''\!.2$
Observing duration (hrs)	8	4.5[†]
Range of baselines (km)	0.1–25	0.1–11
Observing frequency (MHz)	1395.00	1640.22
Bandwidth per IF (MHz)	8.0	6.25
Number of spectral channels	128	128
Polarizations	2	1
Frequency resolution (kHz)	62.5	48.8
Velocity resolution (km s^{-1})	13.7	9.0
Amplitude calibrator	0137+331	0137+331
Phase calibrator	0137+331	0137+331
Bandpass calibrator	0137+331	0137+331

[†] Usable time, see Sect. 3.2 for details.

of 4400−5550 km s^{-1} for the 1667 MHz line of OH with a velocity resolution of ~9 km s^{-1}. These observations also covered the 1665 MHz line of OH in the velocity range of 4050−5200 km s^{-1}. A large fluctuation in the system temperature was noticed on the first day of observations which were carried out at a centre frequency of 1640.5 MHz. These fluctuations were later identified as due to strong signals from a external interfering source operating near the frequency of observations. The observations on the next day were carried out after reducing the front-end bandwidth from 25 MHz to 12.5 MHz

and shifting the centre of the band to 1640.22 MHz to avoid the external interference. The data from the first day of observations were discarded.

The VLA observations and data analyses were carried out following the same strategy as adopted for the GMRT observations described in Sect. 3.1. The flux density of 3C 48 was estimated to be 14.270 Jy at the observing frequency. The image cube was generated using "natural-weighted" continuum-free data to get maximum signal to noise ratio. The image cube was box-car smoothed along the frequency axis using a window of
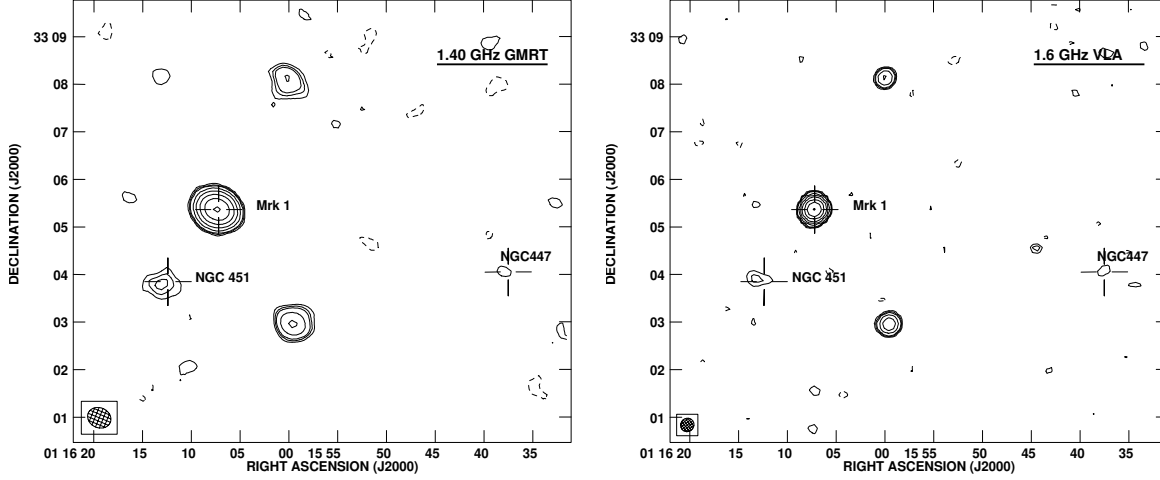
Fig. 1. Radio continuum images of the group WBL 035. The image in the left panel is at 1.4 GHz from the GMRT and that at the right panel is at 1.6 GHz from the VLA. The crosses mark the optical positions of the members of the group. The contours are drawn as -1, 1, 1.5, 2, 4, 8, 16, 32, 64, 128 in units of 1.1 mJy beam^{-1} at 1.4 GHz and in units of 0.5 mJy beam^{-1} at 1.64 GHz respectively. The synthesized beam, shown in the bottom left hand corner, is $30\rlap{.}''75 \times 25\rlap{.}''17$, PA = $+67.8°$ in the 1.4 GHz image; and $17\rlap{.}''49 \times 16\rlap{.}''56$, PA = $-52.0°$ in the 1.6 GHz image. The images are corrected for respective primary beam attenuations. The rms noise is 0.35 mJy beam^{-1} in the 1.4 GHz image and 0.19 mJy beam^{-1} in the 1.6 GHz image. The peak flux densities in the images are 76.3 mJy beam^{-1} at 1.4 GHz and 68.1 mJy beam^{-1} at 1.6 GHz.

3 channels and every second channel was discarded. The resulting image cube has a resolution of $5\rlap{.}''43 \times 4\rlap{.}''93 \times 27$ km s^{-1}. The continuum images were made using the self-calibrated averaged data from the line-free channels.

4. Results

4.1. Radio continuum

The radio continuum images shown in Fig. 1 have a resolution of $30\rlap{.}''75 \times 25\rlap{.}''17$ at 1.4 GHz, and $17\rlap{.}''49 \times 16\rlap{.}''56$ at 1.6 GHz. These images were made using only short (u, v) spacings to enhance the sensitivity to extended features. These images have an rms of 0.35 mJy beam^{-1} at 1.4 GHz, and 0.19 mJy beam^{-1} at 1.6 GHz. Continuum emission is detected from both Mrk 1 and NGC 451. NGC 447 is marginally detected ($\sim 4\sigma$) at both 1.4 and 1.6 GHz. The flux density of Mrk 1 is estimated to be 76 ± 4 mJy at 1.4 GHz, and 68 ± 3 mJy at 1.6 GHz. The spectral index between 1.4 and 1.6 GHz is 0.8. The flux density of NGC 451 is 3.3 ± 0.5 mJy at 1.4 GHz and 1.8 ± 0.4 mJy at 1.6 GHz. Mrk 1 remains unresolved down to a resolution of ~ 1 kpc.

4.2. H I emission

The H I cube was made with a resolution of $30\rlap{.}''67 \times 27\rlap{.}''28 \times 13.7$ km s^{-1}. The channel images have an rms of 0.92 mJy beam^{-1}. The corresponding 3σ sensitivity in H I column density is 5.0×10^{19} cm^{-2}. The channel images of H I emission and absorption are shown in Figs. 2 and 3. The results are summarized in Table 3. H I emission is detected in the velocity range of 4698 to 4984 km s^{-1}. H I emission from Mrk 1 appears from 4698 to 4848 km s^{-1}. The flux integral ($\int S$ dV) of H I emission in this range is 0.73 ± 0.05 Jy km s^{-1}

Table 3. Radio continuum and H I emission results.

Parameter	Mrk 1	NGC 451
$S^{(\text{cont.})}_{1.4\ \text{GHz}}$ (mJy)	76 ± 4	3.3 ± 0.5
$S^{(\text{cont.})}_{1.6\ \text{GHz}}$ (mJy)	68 ± 3	1.8 ± 0.4
$\delta V^{(\text{H I emission})}$ (km s^{-1})	120	170
Systemic velocity (km s^{-1})	4780 ± 13[†]	4897 ± 2[‡]
Maximum rot. velocity (km s^{-1})	–	140[‡]
Inclination (degree)	–	31 ± 10[‡]
H I extent (kpc)	~ 30	~ 20
$\int S^{(\text{H I emission})}$ dV (Jy km s^{-1})	0.73 ± 0.05	1.2 ± 0.1
H I mass ($10^8\ M_\odot$)	8.0 ± 0.6	13 ± 1.0

[†]: Estimated from the mean velocity of H I emission.
[‡]: Estimated from a fit of curves of constant velocities to the H I velocity field.

which at the distance of Mrk 1 corresponds to a total H I mass of $8.0(\pm 0.6) \times 10^8\ M_\odot$ for Mrk 1. The estimated HI mass is a lower limit due to the effects of absorption. H I emission from NGC 451 is detected from 4807 to 4984 km s^{-1} with a total flux integral of 1.20 ± 0.10 Jy km s^{-1} corresponding to a H I mass of $1.31(\pm 0.11) \times 10^9\ M_\odot$ assuming a distance to NGC 451 of 68 Mpc. The summed flux integral of Mrk 1 and NGC 451 is $1.93(\pm 0.11)$ Jy km s^{-1}, which is consistent with the value obtained by the single dish observations of Hutchings (1989). See Fig. 4 for a global H I profile.

The moment zero map shown in Fig. 5 indicates that the H I emission from Mrk 1 is distributed in three clumps with almost all H I seen outside the optical extent of Mrk 1. The individual clumps having velocity dispersions of 30 to 60 km s^{-1} are distributed over an extent of ~ 30 kpc. The velocity field of Mrk 1
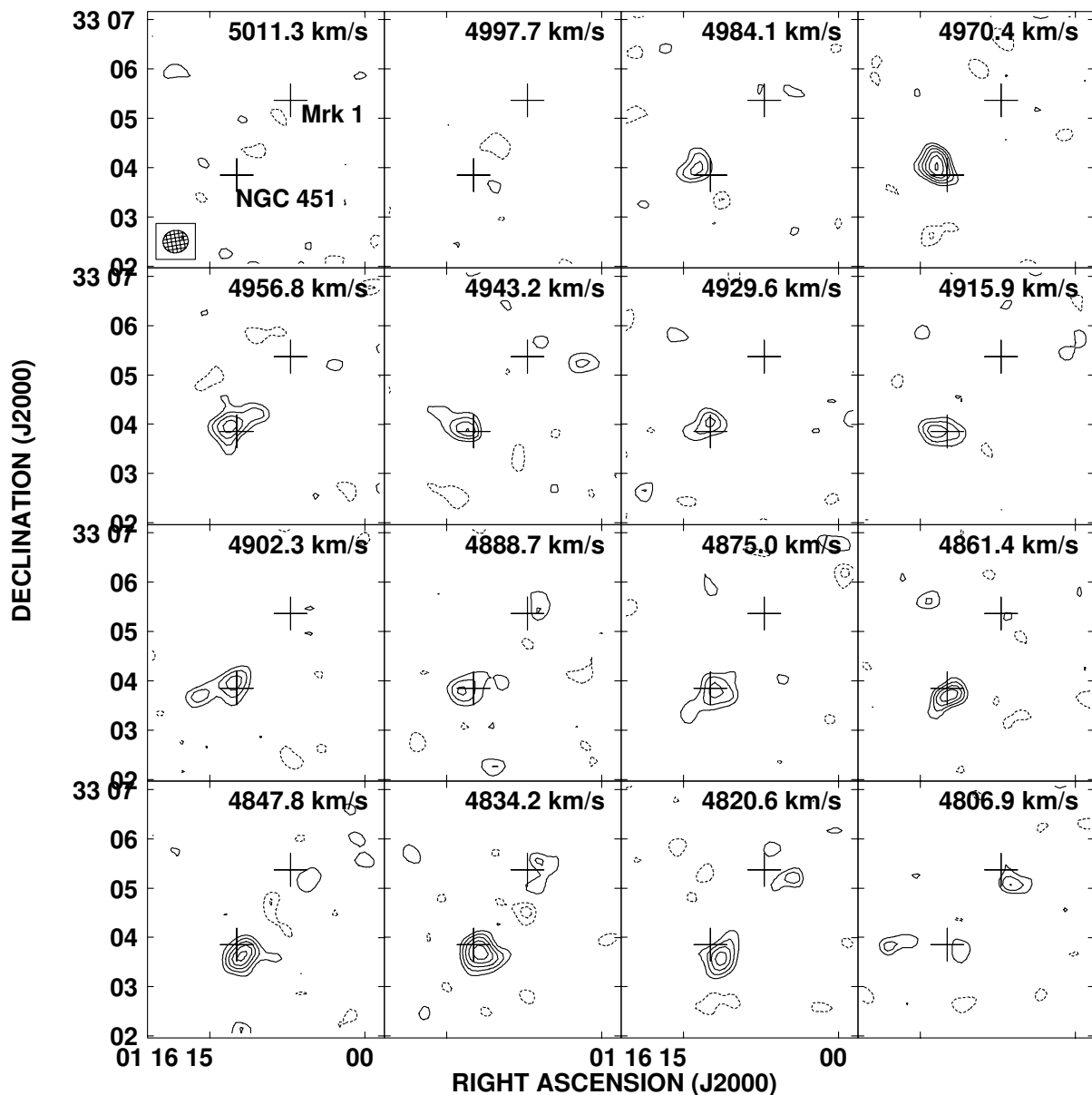
Fig. 2. Channel images from GMRT showing H I column density contours in the velocity range 4807 km s^{-1}–5011 km s^{-1}. The crosses mark the optical positions of Mrk 1 and NGC 451. Solid contours representing column density of H I emission are drawn at 3.6, 5.4, 7.2, 9.0, 10.8, and 12.7 × 10^{19} cm^{-2}. The negative contours (dashed curves) are drawn at 2, 3, 4, 5, 6 mJy beam^{-1}. The HPBW of the synthesized beam (30.″67 × 27.″28, PA = −80.4°) is indicated at the bottom left hand corner of the first channel image. The velocity resolution in the cube is ∼13.7 km s^{-1}.

shown in Fig. 6 indicates that there is a smooth rotation of H I from one end to the other.

The H I emission from NGC 451 shown in Fig. 5 looks like that of a disk galaxy with a total projected velocity width of 170 km s^{-1}. The H I diameter of NGC 451 is ∼20 kpc which is about twice that of the optical disk. The global parameters of NGC 451 given in Table 3 were derived from a fit to the velocity field made using a higher resolution (17″ × 14″) H I cube which is not shown here.

4.3. H I absorption

The channel images shown in Fig. 3 also show H I absorption from Mrk 1 (dotted contours at the location of Mrk 1) in the velocity range 4589 km s^{-1} to 4752 km s^{-1}. The H I absorption spectrum shown in Fig. 7 is extracted at the radio position of Mrk 1 from a H I cube made with a resolution of 6.″23 × 4.″39 × 13.7 km s^{-1}. The rms in this cube was 0.6 mJy beam^{-1}. The spectrum shows a broad
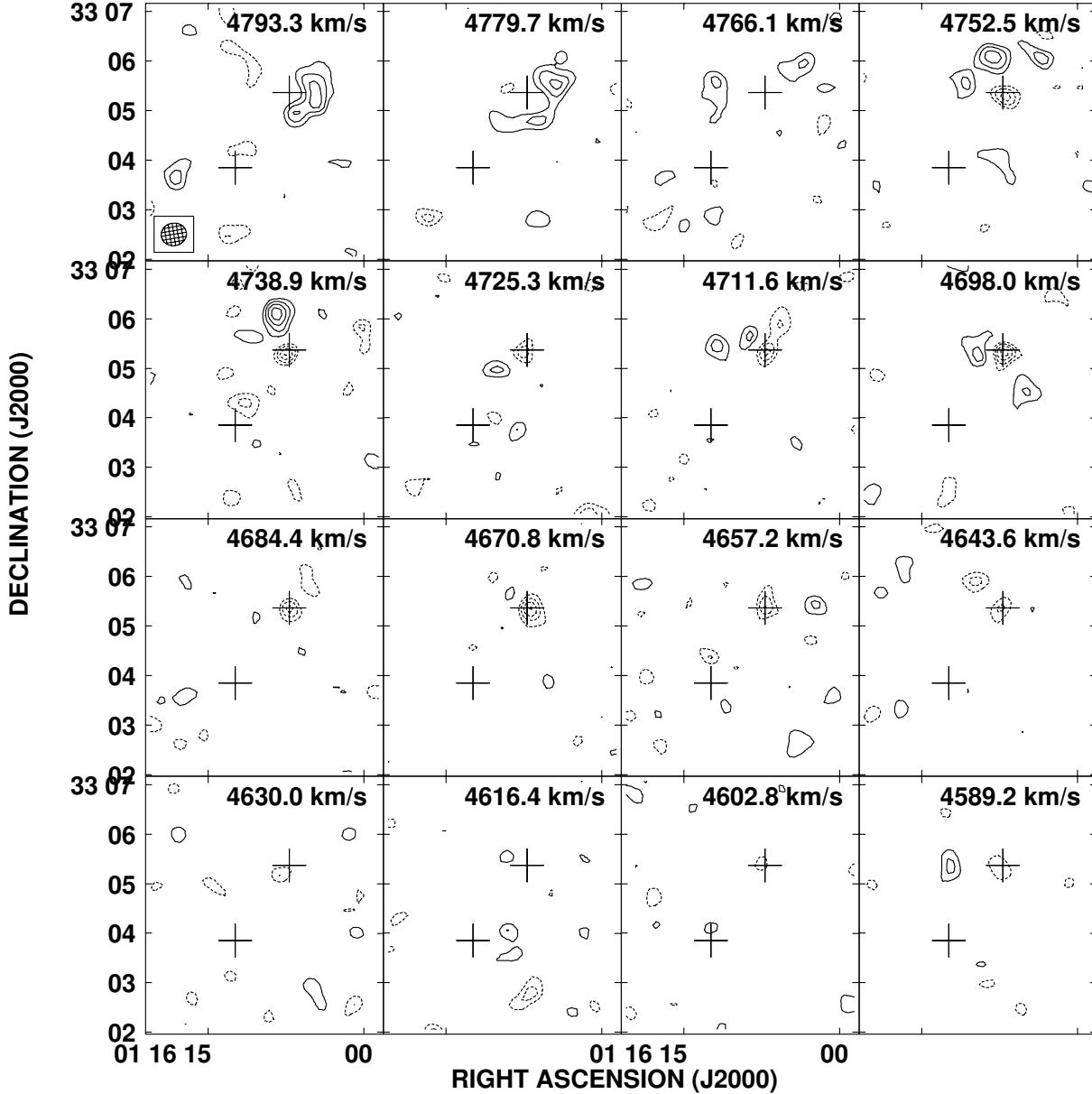
Fig. 3. Channel images showing column density contours in the velocity range 4589 km s^{-1}–4793 km s^{-1}. The contour levels are the same as in Fig. 2. The Hi absorption is seen toward Mrk 1 as dotted contours.

multi-component absorption in between the velocities 4500 km s^{-1} and 4800 km s^{-1}. Two Gaussian components were fitted to the Hi absorption profile. The resulting parameters of the fit are given in Table 4. The peak optical depths of the two components are 0.073 ± 0.004 and 0.032 ± 0.004 respectively and the velocity dispersions are $\sim$44 km s^{-1} for both the components. The column density of Hi is estimated using the relation $N_{\mathrm{H I}} = 1.82 \times 10^{18} \times (T_{\mathrm{spin}}/f) \int \tau \, \mathrm{d}v$ cm^{-2}; where T_{spin} is the spin temperature of Hi in Kelvin, f is the covering fraction of Hi gas, $\int \tau \, \mathrm{d}v$ is the velocity integrated optical depth in km s^{-1}. We assume f to be unity. T_{spin} is an unknown

quantity and we adopt a value of 100 K, typical of cold clouds in our Galaxy. The Hi column densities are then $1.5(\pm0.2) \times 10^{21}$ cm^{-2} and $6.0(\pm1.5) \times 10^{20}$ cm^{-2} for the two components respectively.

4.4. OH absorption

The OH spectrum shown in Fig. 8 was extracted at the radio position of Mrk 1 from the image cube made using the VLA data with a resolution of $5''43 \times 4''93 \times 27$ km s^{-1}. The cube has an rms of 0.5 mJy beam^{-1}.
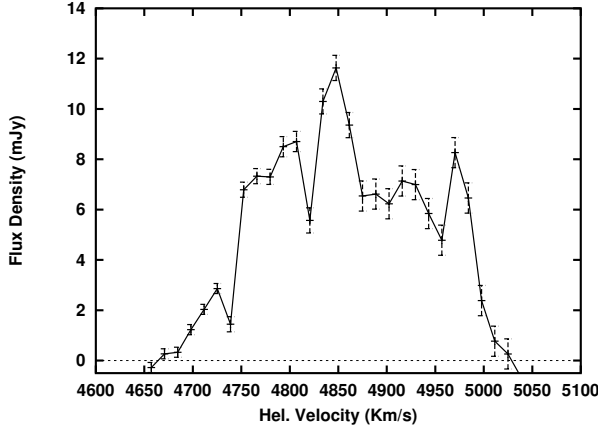
Fig. 4. Global H I emission profile of Mrk 1 and NGC 451 from GMRT. The flux integral is 1.93 ± 0.11 Jy km s^{-1} which is consistent with the single dish observations of Hutchings (1989).
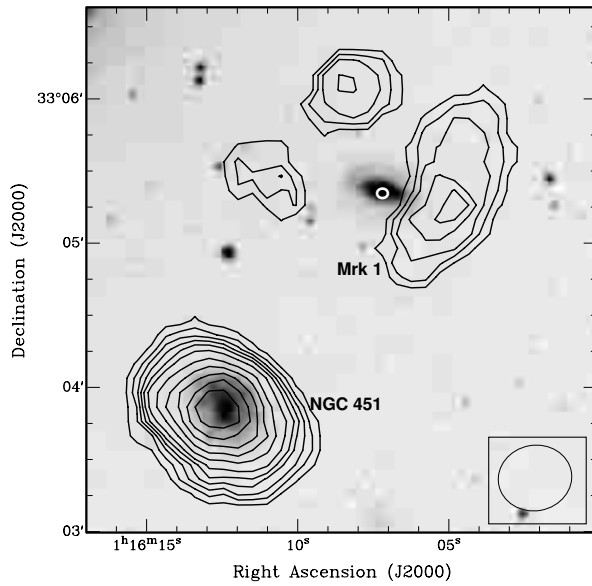

Fig. 5. The column density contours of the total H I image from GMRT of Mrk 1 (top) and NGC 451 (bottom) overlaid upon the grey scale optical image from the DSS (blue). The contour levels are 0.3, 0.8, 1.3, 1.8, 2.3, 3, 4, 5, 6, 7, 8, and 9 in units of 10^{20} cm^{-2}. The HPBW of the synthesized beam, shown in the bottom right hand corner, is $30.''67 \times 27.''28$, PA = $-80.4°$. Although the H I emission is surrounding Mrk 1, H I absorption (marked as white circle) is detected toward Mrk 1 indicating the presence of cold H I gas in front of it.

The velocity axis of Fig. 8 corresponds to the 1667 MHz OH line. In this velocity system, the 1665 MHz line will appear at +360 km s^{-1} from the 1667 MHz line. Since the spectrum of Fig. 8 does not have enough baseline for the 1667 MHz line and not enough signal to noise ratio for both the 1665 MHz line to get reliable estimates for velocity dispersions of individual components, only peak optical depths and center velocities were fitted while the velocity dispersions were fixed at those
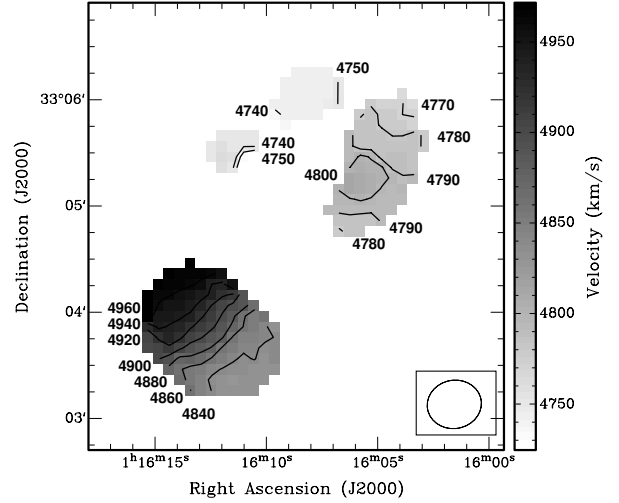

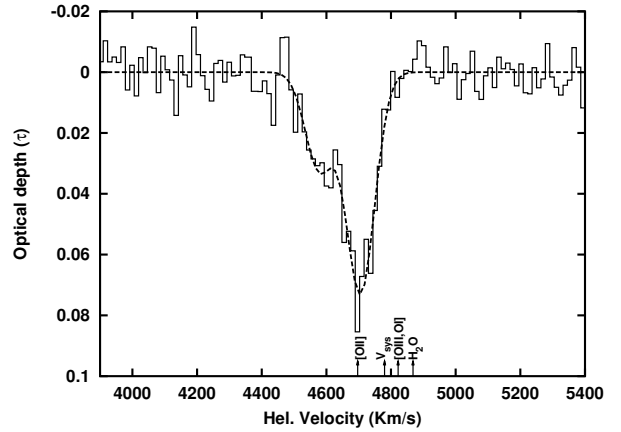**Fig. 6.** The velocity fields of Mrk 1 and NGC 451 from GMRT are shown as contours and in grey scale.

Fig. 7. The GMRT spectrum showing H I absorption in Mrk 1. The dotted curve is the Gaussian fit to the absorption spectrum. The fitted parameters are given in Table 4. The vertical lines along the velocity axis mark the positions of several velocity systems as indicated.

Table 4. H I and OH absorption results.

Parameter	H I	OH(1667)	OH(1665)
τ_1	0.073 ± 0.004	0.023 ± 0.003	0.014 ± 0.004
v_1 (km s^{-1})	4705 ± 5	4721 ± 6	4710 ± 19
σ_{v_1} (km s^{-1})	44.2 ± 4.4	44.2	44.2
τ_2	0.032 ± 0.004	0.011 ± 0.003	0.006 ± 0.004
v_2 (km s^{-1})	4579 ± 10	4585 ± 12	4601 ± 45
σ_{v_2} (km s^{-1})	43.4 ± 9.1	43.4	43.4

values found in fitting the H I absorption profile. This is a reasonably good assumption since both the 1665 and 1667 MHz profiles are qualitatively similar to the H I absorption profile. This procedure gave a reasonably good, though not unique, fit to the OH spectrum. The fitted parameters are given in Table 4.
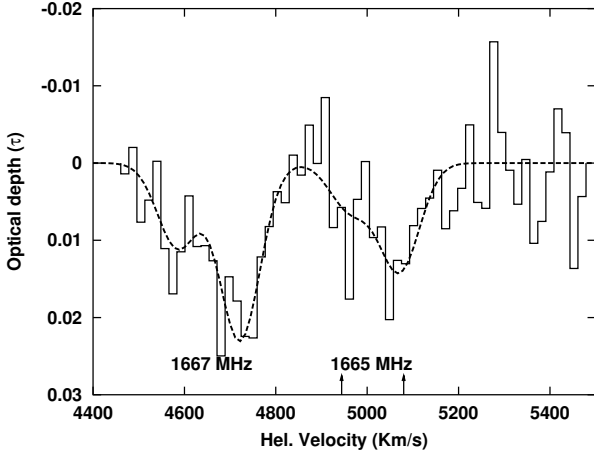
Fig. 8. The VLA spectrum showing OH absorption from Mrk 1. The velocity axis corresponds to the 1667 MHz line. The dotted curve shows the model spectrum of the 1665 and 1667 MHz OH lines. The fitted parameters are given in Table 4. In this velocity definition, the 1665 MHz line will appear at $+360$ km s^{-1} from the 1667 MHz line. Two vertical lines in the velocity axis mark the expected positions of 1665 MHz absorption corresponding to the 1667 MHz absorption detected near 4721 and 4585 km s^{-1}.

Table 5. Interaction properties of the Mrk 1–NGC 451 system.

Parameter	Value
Projected velocity difference (km s^{-1})	117
Projected separation (kpc)	38
Total dynamical mass ($M_\odot$)	$\sim 10^{11}$
Tidal radius (Mrk 1) (kpc)	24
Tidal radius (NGC 451) (kpc)	29
Impact parameter	~ 0.1
Dynamical friction time (Gyr)	~ 0.2
Orbital time (Gyr)	~ 2.0

The peak optical depths of the two components of the 1667 MHz absorption are 0.023 ± 0.003 and 0.011 ± 0.003 respectively. The column density of OH is estimated using the relation $N_{\mathrm{OH}} = 2.35 \times 10^{14} \times (T_{\mathrm{ex}}/f) \int \tau_{1667} \, \mathrm{d}v$ cm^{-2}; where T_{ex} is excitation temperature which is assumed to be 10 K and $\int \tau_{1667} \, \mathrm{d}v$ is the velocity integrated optical depth of the 1667 MHz line in units of km s^{-1}. The OH column densities are estimated to be $6.0(\pm 1.0) \times 10^{15}$ cm^{-2} and $2.9(\pm 0.9) \times 10^{15}$ cm^{-2}. The peak optical depth ratio τ_{1667}/τ_{1665} of the stronger OH component is 1.6 ± 0.5, indicating that this component is excited under LTE conditions – the ratio is predicted to be in between 1.0 and 1.8 for LTE excitations. This ratio for the weaker component, viz., 1.8 ± 1.3 indicates that this is also most likely thermally excited.

5. Discussion

5.1. Interaction of Mrk 1 with NGC 451

The disturbed H I morphology of Mrk 1 (Fig. 5) indicates a gravitational interaction possibly with the nearest companion NGC 451. We explore this possibility using the two body interaction described in Binney & Tremaine (1987). The dynamical masses of galaxies are estimated using rotation curves. Since the H I morphology of Mrk 1 is disturbed, it was not possible to obtain a reliable H I rotation curve. We used the Hα rotation curve of Mrk 1 (Keel 1996). The dynamical mass of NGC 451 was estimated using the H I rotation curve. The dynamical masses of Mrk 1 and NGC 451 are 3.4×10^{10} $M_\odot$ and 4.5×10^{10} $M_\odot$ respectively. The interaction parameters are listed in Table 5.

The projected velocity difference between Mrk 1 and NGC 451 of ~ 117 km s^{-1} indicates the minimum dynamical

mass of this pair to be $\sim 10^{11}$ $M_\odot$. This value of dynamical mass is in close agreement with the dynamical masses of Mrk 1 and NGC 451, indicating that Mrk 1 and NGC 451 are most likely in a bound system. Tidal radii (cf. Eq. (7–84), Binney & Tremaine 1987) for the given masses of Mrk 1 and NGC 451 indicate that the outer regions of the H I disk of Mrk 1 can be perturbed easily. The dynamical friction time scale (cf. Eq. (7–26) and (7–13b), Binney & Tremaine 1987) of ~ 0.2 Gyr for this system is much smaller than their orbital time scale of ~ 2 Gyr. This implies that the interaction is bound and will lead to a merger within a small fraction of the orbital time period of the two galaxies.

5.2. Comparison of H I and OH velocities with other velocity systems

Comparison with optical line velocities – from the comparison of the H I and OH absorption velocities of Mrk 1 with the optical line velocities listed in Table 1, it appears that the higher velocity components of the H I and OH absorption are consistent with the [O II]λ3727 line velocity, but are blueshifted by ~ 100 km s^{-1} from the [O III]λ5007, [O I]λ6300 and the systemic velocity. We explain this discrepancy in terms of co-existence of photo-ionized and shock ionized gas in active galaxies. The [O III]λ5007 line is primarily due to excitation from a hard continuum, and therefore, should be arising close to the nucleus. The [O II]λ3727 line intensity is enhanced in shock ionized regions (Dopita & Sutherland 1995). Most often, optical line profiles are asymmetric and only peak line velocities are quoted without fitting a line profile. Mrk 1 is known to be such a case (Bergeron & Durret 1987; Dickinson et al. 1976). Such an analysis of the optical spectrum may bias the line velocities of different species toward different regions, e.g., the peak of the [O II] line may indicate a region which is shock ionized while the [O III] line velocity may indicate gas which is close to the nucleus. We speculate that the higher velocity H I and OH absorption component in Mrk 1 arises in a region which is pushed forward due to shocks, thereby giving an apparent blueshift to H I, OH, and [O II] lines. The fact that the [O I] line velocity is close to the [O III] line velocity, and hence associated with photo-ionized regions, is not surprising since the [O I] line intensity is suppressed in the shock excited regions (Dopita & Sutherland 1995).

Table 6. Properties of the absorbing gas.

Parameter	Value
$N_1(\text{H\,I})^{\dagger}$ (cm^{-2})	$1.5(\pm0.2) \times 10^{21}$
$N_2(\text{H\,I})^{\dagger}$ (cm^{-2})	$6.0(\pm1.5) \times 10^{20}$
$N_1(\text{OH})^{\ddagger}$ (cm^{-2})	$6.0(\pm1.0) \times 10^{15}$
$N_2(\text{OH})^{\ddagger}$ (cm^{-2})	$2.8(\pm1.0) \times 10^{15}$
$N_{\text{total}}(\text{H\,I})$ (cm^{-2})	$2.1(\pm0.6) \times 10^{21}$
$N_{\text{total}}(\text{OH})$ (cm^{-2})	$8.8(\pm3.4) \times 10^{15}$
$\tau_{\text{H\,I}}/\tau_{\text{OH, 1667}}$ (1)	3.2 ± 0.4
$\tau_{\text{H\,I}}/\tau_{\text{OH, 1667}}$ (2)	2.9 ± 0.9
$\tau_{\text{OH, 1667}}/\tau_{\text{OH, 1665}}$ (1)	1.6 ± 0.5
$\tau_{\text{OH, 1667}}/\tau_{\text{OH, 1665}}$ (2)	1.8 ± 1.3
$N_{\text{total}}(\text{H}_2)^{\dagger\dagger}$ (cm^{-2})	$\sim10^{23}$
$N_{\text{total}}(\text{OH})/N_{\text{total}}(\text{H\,I})$	$\sim4.3 \times 10^{-6}$
A_{v} (mag)	9–90
N_{H} cm^{-2}	$\sim1.1 \times 10^{23}$
$\tau_{\text{photoelectric}}^{1\text{keV}}$	~30

†: Assuming T_{spin} = 100 K; ‡: Assuming T_{ex} = 10 K; ††: Assuming OH/H$_2$ = 10^{-7}.

Comparison with H$_2$O megamaser and CO emission – the water megamasers are seen from Mrk 1 at a velocity of 4868 km s^{-1} (Braatz et al. 1994). Since these masers are red-shifted by $\sim$90 km s^{-1} from the systemic velocity of the galaxy, they are most likely the high velocity "satellite" features commonly seen in water megamaser galaxies (Braatz et al. 1997) and thought to originate in the accretion disks near the nuclei (Neufeld et al. 1994). Since the observed H\,I and OH absorption velocities in Mrk 1 are blueshifted from both the water megamaser velocity and from the systemic velocity of the galaxy, the absorption in the present case is most likely not related either to the gas in the accretion disk or to the torus close to the nucleus. The mean velocity of the CO emission from Mrk 1 is 4850 km s^{-1} (Vila-Vilaro et al. 1998), which is red-shifted by $\sim$150 km s^{-1} from H\,I and OH absorption velocities, implying that the gas traced via H\,I and OH absorption in Mrk 1 is also not related to the molecular gas traced by CO emission.

5.3. Kinematics and composition of the absorbing gas

The general properties of the gas seen in absorption are summarized in Table 6. The total column density of OH is comparable to that observed in other active galaxies (e.g., Schmelz et al. 1986; Baan et al. 1985, 1992). Both components of the OH transitions appear to be thermally excited as their optical depth ratios (τ_{1667}/τ_{1665}) are between 1.0 and 1.8; the values predicted for excitations in LTE conditions. The optical depth ratios $\tau_{\text{H\,I}}/\tau_{\text{OH}}$ for both the components of the absorbing gas are $\sim$3. This ratio has been found to be varying from as low as 5 to more than 400 in Galactic clouds (Dickey et al. 1981). The smaller values correspond to the molecular clouds while larger values correspond to the diffuse clouds. It is therefore suggested that the H\,I and OH absorption, in the present case, are associated with dense molecular clouds.

The observed velocity dispersion (σ) of the 1667 MHz OH absorption, viz., 44 km s^{-1} is higher than the typical velocity dispersions (σ = 3–7 km s^{-1}) in giant molecular clouds (GMCs) of the Galactic disk. However, several high dispersion clouds (σ $\sim$ 40 km s^{-1}) have been detected in 18 cm OH absorption within a kpc of the Galactic centre (Boyce & Cohen 1994). The simplest explanation for such a high velocity dispersion could be a chance alignment of several normal GMCs along the line of sight, but Kumar & Riffert (1997) have shown that the probability of such alignments is small. Alternatively, if the velocity dispersion is due to a single gravitationally bound system in virial equilibrium, the mass of such an object (assuming a size of 50 pc) could be $\sim$10^7 $M_{\odot}$. Cloud–cloud collisions (Klein et al. 1994b) and interaction of shock with ISM (Klein et al. 1994a) are also known to enhance the internal velocity dispersions of molecular clouds.

The OH column density is known to correlate with the visual extinction, A_{v}, of molecular clouds in our Galaxy (Magnani et al. 1988). Magnani et al. (1988) found that $N(\text{OH})/A_{\text{v}}$ ratios are in the range of 10^{14}–10^{15} cm^{-2} mag^{-1}. For the OH column density toward Mrk 1, these ratios indicate $9 < A_{\text{v}} < 90$ toward the line of sight of Mrk 1. In comparison, Veilleux et al. (1997), based on some infrared measurements, obtained a lower limit on A_{v} to be 26 consistent with above predictions.

Using OH/H$_2$ = 10^{-7} (Liszt & Lucas 1996), the implied column density of H$_2$ is $\sim$10^{23} cm^{-2}. Using values of the photo-electric absorption cross sections from Morrison & McCammon (1983) for a gas having the solar abundance, a total hydrogen column density of $\sim$10^{23} cm^{-2} indicates that the optical depth for X-ray absorption at 1 keV will be $\sim$30. Such a high value of the optical depth will absorb almost all soft X-ray radiation from the nucleus of Mrk 1. Consistent with this prediction, Mrk 1 has not been detected as a X-ray source down to a sensitivity of $\sim$10^{41} erg s^{-1} (Fabbiano et al. 1992).

6. Conclusions

We have presented the observations of the Seyfert 2 galaxy Mrk 1 in the H\,I 21 cm line using the GMRT and in the OH 18 cm line using the VLA. Unlike the optical morphology, the H\,I emission morphology of Mrk 1 indicates that this galaxy is disturbed which we interpret as due to tidal interactions with the nearby companion NGC 451. We also showed based on the dynamical study of Mrk 1 – NGC 451 system that the interaction is bound leading to a merger within a small fraction of their orbital time period. This is consistent with the hypothesis that the bound interactions should be more efficient in triggering nuclear activities than unbound interactions. The H\,I and OH absorption detected toward the nucleus of Mrk 1 indicates an outflow of both atomic and molecular gas. The column densities of the detected H\,I and OH absorption indicate that the line of sight toward the nucleus of Mrk 1 is rich in both atomic and molecular gas. The gas detected in absorption is kinematically different than that traced via CO emission and water megamaser emission from Mrk 1. We found evidences that shocks (presumably due to nuclear activities) can affect the kinematics of gas near the nucleus. The H\,I and OH absorption being blueshifted from the systemic velocity and the [O\,III]λ5007

414   A. Omar et al.: Mrk 1 – GMRT and VLA observations

velocity while consistent with the [O ɪɪ]λ3727 velocity is understood in terms of the shock ionization of gas (which predicts enhancement of the [O ɪɪ] line intensity) and an outflow of ISM in front of the shock. Based on the optical depth ratios and the line widths of the H ɪ and OH absorption, we speculate that the absorption is arising in turbulent molecular clouds of similar types as those found near the Galactic centre. These observations also imply that the line of sight toward the nucleus of Mrk 1 is heavily obscured.

References

Baan, W. A., Haschick, A. D., Buckley, D., & Schmelz, J. T. 1985, AJ, 293, 394
Baan, W. A., Haschick, A. D., & Henkel, C. 1992, AJ, 103, 728
Bergeron, J., & Durret, F. 1987, A&A, 184, 93
Binney, J., & Tremaine S. 1987, Galactic Dynamics (Princeton Univ. Press, Princeton, NJ)
Boyce, P. J., & Cohen, R. J. 1994, A&AS, 107, 563
Braatz, J. A., Wilson, A. S., & Henkel, C. 1994, ApJ, 437, L99
Braatz, J. A., Wilson, A. S., & Henkel, C. 1997, ApJS, 110, 321
Dahari, O. 1984, AJ, 89, 996
De Robertis, M. M., Yee, H. K. C., & Hayhoe, K. 1998, ApJ, 496, 93
De Robertis, M. M., & Shaw, R. A. 1990, ApJ, 348, 421
Dickey, J. M., Crovisier, J., & Kazès, I. 1981, A&A, 98, 271
Dickinson, D. F., Kojoyan, G., Purton, C. R., Sramek, R. A., & Tovmassian, Kh. M. 1976, Astron. Nachr. 1976, 297, 283
Dopita, M. A., & Sutherland, R. S. 1995, ApJ, 455, 468
Fabbiano, G., Kim, D. W., & Trinchieri, G. 1992, ApJS, 80, 531
Gallimore, J. F., Baum, S. A., O'Dea, C. P., Pedlar, A., & Brinks, E. 1999, ApJ, 524, 684
Hernquist, L., & Mihos, J. C. 1995, ApJ, 448, 41
Hutchings, J. B. 1989, AJ, 98, 524
Kay, L. E. 1994, ApJ, 430, 196
Keel, W. C. 1996, AJ, 111, 696
Klein, R. I., McKee, C. F., & Collela, P. 1994a, 1994, ApJ, 420, 213
Klein, R. I., McKee, C. F., & Woods, D. T. 1994b, in ASP Conf. Ser., 80, 366
Koski, A. T. 1978, ApJ, 223, 56
Kukula, M. J., Ghosh, T., Pedlar, A., & Schilizzi, R. T. 1999, ApJ, 518, 117
Kumar, P., & Riffert, H. 1997, MNRAS, 292, 871
Liszt, H., & Lucas, R. 1996, A&A, 314, 917
Magnani, L., Blitz, L., & Wouterloot, J. G. A. 1988, ApJ, 326, 909
Markarian, B. E., Lipovetsky, V. A., Stepanian, J. A., Erastova, L. K., & Shapovalova, A. I. 1989, Sobshcheniya Spetsialnoi Astrof. Obs., 62, 5
Morganti, R., Oosterloo, T., & Tsvetanov, Z. 1998, AJ, 115, 915
Morrison, R., & McCammon, D. 1983, AJ, 270, 119
Neufeld, D. A., Maloney, P. R., & Conger, S. 1994, ApJ, 436, L127
Schmelz, J. T., Baan, W. A., Haschick, A. D., & Eder, J. 1986, AJ, 92, 1291
Simkin, S. M., van Gorkom, J., Hibbard, J., & Su, H. 1987, Science, 235, 1367
Swarup, G., Ananthakrishnan, S., Kapahi, V. K., et al. 1991, Curr. Sci., 60, 95
Tadhunter, C., Wills, K., Morganti, R., Oosterloo, T., & Dickson, R. 2001, MNRAS, 327, 227
Veilleux, S., Goodrich, R. W., & Hill, G. J. 1997, ApJ, 477, 631
Vila-Vilaro, B., Taniguchi, Y., & Nakai, N. 1998, AJ, 116, 1553
Weedman, D. W., & Khachikyan, E. E. 1968, Astrophysics, 4, 243
White, R. A., Bliton, M., Bhavser, S. P., et al. 1999, AJ, 118, 2014